DEVELOPMENT OF GRAPHENE SUPPORTED CATALYST NANOPARTICLES FOR POLYMER ELECTROLYTE MEMBRANE (PEM) FUEL CELLS

by
VILDAN BAYRAM

Submitted to the Graduate School of Engineering and Natural Sciences

in partial fulfillment of

the requirements for the degree of

Master of Science

Sabanci University
July 2015

DEVELOPMENT OF GRAPHENE SUPPORTED CATALYST NANOPARTICLES FOR POLYMER ELECTROLYTE MEMBRANE (PEM) FUEL CELLS

APPROVED BY:

Assoc. Prof. Selmiye Alkan Gürsel (Thesis Supervisor).....

Assist. Prof. Oktay Demircan…….....

Assist. Prof. Gözde Özaydın İnce.....

DATE OF APPROVAL: ……

DEVELOPMENT OF GRAPHENE SUPPORTED CATALYST NANOPARTICLES FOR POLYMER ELECTROLYTE MEMBRANE (PEM) FUEL CELLS

VILDAN BAYRAM

MAT, M.Sc. Thesis, 2015

Thesis Supervisor: Assoc. Prof. Selmiye Alkan Gürsel

Keywords: Graphene, Catalyst Impregnation Methods, Catalyst Nanoparticles, Electrode Layer, PEMFC

ABSTRACT

Catalyst nanoparticles inside PEM fuel cells are generally supported with a powdered material which has a high surface area, high mechanical and thermal stability, and preferably high conductivity. Vulcan®XC-72 which is a type of carbon black (CB) is the most conventional material that is used as catalyst support. It has a BET specific surface area of 250 $m^2.g^{-1}$ and conductivity of 4-7.4 $S.cm^{-1}$. The usage of CB in fuel cells is beneficial in terms of this tempting features, however, the lack of tolerance to carbon monoxide (CO) poisoning due to the presence of deep cracks in its structure creates a great problem inside a harsh fuel cell environment. Graphene, on the other hand, provides a large surface area and high conductivity while providing a large and stable surface support as a result of its two dimensional structure. In this thesis study, the influence of using graphene derivatives (graphene oxide (GO), thermally reduced GO (TRGO) and

graphene nanoplatelets(GNP)) as catalyst support materials to the catalytic activity of platinum (Pt) nanoparticles and fuel cell performance was evaluated in combination with the utilization of various platinum impregnation methods (ascorbic acid, ethylene glycol reflux, sodium borohydride reduction). The synthesized materials were characterized by using XRD, Raman, FTIR, TEM, SEM, Cyclic Voltammetry (CV), BET Surface Area Analysis, XPS and Fuel Cell Performance Test. Ethylene glycol method and GO were determined to be the most effective impregnation method and the best catalyst support candidate respectively. Ethylene glycol reflux was further applied to impregnate Pt on Vulcan®XC-72.The results were compared with commercial Vulcan®XC-72 supported Pt nanoparticles and synthesized Pt/ Vulcan®XC-72.

POLİMER ELEKTROLİT MEMBRANLI YAKIT PİLLERİ İÇİN GRAFEN DESTEKLİ NANOPARÇACIK KATALİZÖRLERİN GELİŞTİRİLMESİ

Vildan Bayram

MAT, M.Sc. Tezi, 2015

Tez Danışmanı: Doç. Dr. Selmiye Alkan Gürsel

Anahtar Kelimeler: Grafen, Katalizör Üretim Yöntemleri, Katalizör Nanoparçacıklar, PEM Yakıt Pili

ÖZET

PEM yakıt pilleri içerisindeki katolizerler genellikle yüksek yüzey alanına, ısıl ve mekanik dayanlıklılığa, ve tercihen yüksek iletkenlikteki toz malzemeler tarafından desteklenmektedir. Çoğunlukla bu amaç için bir karbon siyahı (CB) türevi olan Vulcan®XC-72 kullanılmaktadır. BET yüzey alanı 250 $m^2.g^{-1}$ ve iletkenliği 4-7.4 $S.cm^{-1}$ olan Vulcan®XC-72, bu amaç için oldukça uygundur. Ancak yapısında bulunan derin çatlaklar sebebiyle ağır yakıt pili koşullarında karbon monoksit (CO) zehirlenmesine neden olmaktadır. Öte yandan grafen, yüksek iletkenlik ve yüzey alanına sahip olmasının yanında iki boyutlu yapısı sayesinde dayanıklı bir yüzey desteği sağlamaktadır. Bu tez çalışmasında, grafen türevlerinin (grafen oksit (GO), ısıl olarak indirgenmiş GO (TRGO) ve grafen levhaları (GNP)) platin (Pt) nanoparçacıklarının elektrokatalitik aktiviteleri ve yakıt pili performansı üzerindeki etkileri, çeşitli Pt indirgeme methodlarının (askorbik

asit, etilen glikol geriakımı, sodium borhidrür indirgemesi) kullanımı ile birlikte değerlendirilmiştir. Sentezlenen malzemeler XRD, Raman, FTIR, TEM, SEM, Cyclic Voltammetry (CV), BET Yüzey Alanı Analizi, XPS ve yakıt pili performans testi yapılarak incelenmiştir. Sırasıyla, etilen glikol yöntemi ve grafen oksit en etkili indirgeme metodu ve en iyi katalizör desteği olarak belirlenmiştir. Daha sonra, etilen glikol methodu Vulcan®XC-72 üzerine Pt indirgemesi amacıyla da kullanılmıştır. Sonuçlar ticari Pt/ Vulcan®XC-72 ve sentezlenen Pt/ Vulcan®XC-72 ile kıyaslanarak yorumlanmıştır.

Dedicated to my lovely mother, kind-hearted father,
beautiful sister and little cute brother…

ACKNOWLEDGEMENTS

I immensely would like to thank my supervisor Assoc. Prof. Selmiye Alkan Gürsel for her guidance, endless support, perception and kindness in every case during my graduate studies and research work. I would like to thank my jury member Assist. Prof. Oktay Demircan who was previously my Professor at Bogazici University, for helping to enlarge my chemistry knowledge during my undergraduate years, for his suggestions about my future academic career and finally being a part of my thesis committee. I would like to thank my jury member Assist. Prof. Gözde Özaydın İnce for her precious time reading and editing my thesis, and attending to my thesis defense. Additionally, I would like to thank Assoc. Prof. Burç Mısırlıoğlu and Assoc. Prof. Ersin Acar for their support and guidance during my PhD applications.

I would like to thank Sabanci University providing me with tuition waiver. I would like to show my gratitude to Graphene Flagship as all research work within my master studies has received funding from the European Union Seventh Framework Programme under grant agreement n°604391 Graphene Flagship.

Special thanks to my friends at Sabanci University Begüm Yarar, Veciye Taşcı, Elif Hocaoğlu, Mariamu Kassim Ali, Zaeema Khan, Parveen Qureshi, Atia Shafique, Melike Çokol Çakmak, Asma Almurtadha, Anargül Abliz, Gülben Avşar, Çağatay Yılmaz, Mamuna Ifat. I would like to thank Aslıhan Ünsal for being my partner during my thesis writing process and for her encouraging words when I feel depressed. I especially would like to thank Nesibe Ayşe Doğan and Dilek Çakıroğlu for listening to me when I face with difficulties and always being supportive about my dreams. I would like to thank to my close friends Meryem Şahin and Kübra Bozan for all the laugher and chatter we shared. I would like to thank my dear friend Melike Belenli for being with me since high school and making me happy with her surprisingly positive character. I would like to thank my sincere friend Halenur Karakaya for her affection and wise advice in times of despair and for extreme laughter we share in times of happiness.

I would like to thank Dr. Lale Işıkel Şanlı for helping me organizing my experiments. I would also like to send my thanks to my research group members- Sajjad, Esaam, Sahl, Shayan, Miad, Adnan, Rokhsareh- especially to undergraduate students Ece Arıcı and

Nilay Düzen, for their help, company and friendship during my research. I would like to thank Turgay Gönül and Sibel Pürçüklü for their continuous help throughout my research.

Finally, I would like to thank my family for their continuous help, support and love.

TABLE OF CONTENTS

LIST OF FIGURES

LIST OF TABLES

LIST OF EQUATIONS

ABBREVIATIONS AND SYMBOLS

AFC : Alkaline Fuel Cell

BET : Brunauer–Emmett–Teller

BJH : Barret–Joyner–Halenda

CB : Carbon Black

CE : Counter Electrode

CNT : Carbon Nanotube

CNF : Carbon Nanofiber

CO : Carbon monoxide

CV : Cyclic Voltammetry

CVD : Chemical Vapor Deposition

DMFC : Direct Methanol Fuel Cell

ECSA : Electro Chemical Surface Area

FGS : Functionalized Graphene Sheets

FTIR : Fourier Transform Infrared Spectroscopy

Ge : Germanium,

GDL : Gas Diffusion Layer

GNP : Graphene Nanoplatelets

GNS : Graphene Nanosheets

GO : Graphene Oxide

HDA : Hydrogen Depolarized Anode

HOR : Hydrogen Oxidation Reaction

MCFC : Molten Carbonate Fuel Cell

MEA : Membrane Electrode Assembly

MPC : Mesoporous Carbon

MWCNT : Multi-walled Carbon Nanotube

ORR : Oxygen Reduction Reaction

PAFC : Phosphoric Acid Fuel Cell

PANI : Polyaniline

PDDA : Poly (diallyldimethylammonium chloride)

PEMFC : Polymer Electrolyte Membrane Fuel Cell

PPy : Polypyrrole

Pt : Platinum

PVP : Polyvinylpyrrolidone

RE : Reference Electrode

r-GO : Reduced Graphene Oxide

SEM : Scanning Electron Microscopy

SOFC : Solid Oxide Fuel Cell

SSA : Specific Surface Area

TEM : Transmission Electron Microscopy

TPB : Three Phase Boundary

TRGO : Thermally Reduced Graphene Oxide

XPS : X-ray Photoelecron Spectroscopy

XRD : X-ray Diffraction

1. INTRODUCTION

1.1. Background and Motivation

In the working principle of fuel cell, a catalyst, where electrochemical reactions takes place, should be present inside electrodes. The most efficient catalyst for fuel cells known until now is Platinum (Pt). However, it is not very abundant in nature and very expensive. Pt nanoparticles inside a fuel cell electrode are ordinarily supported by carbon materials. The presence of carbon supporting materials inside electrodes is beneficial in both increasing the dispersion of Pt nanoparticles over electrode layers and decreasing the cost of the electrodes as well as improving the efficiency of the electrochemical reactions. With the appreciable effect of carbon support on properties of electrode layers, selection of carbon support gains a great importance. Carbon black (CB) is the most generally used catalyst support in fuel cells with its high specific surface area and easy production. However, commercially available CBs have many drawbacks such as having deep cracks in their structures which lead to high oxidation rates and carbon monoxide (CO) poisoning during the operation of fuel cells. CBs can be replaced with a better candidate that is graphene which has a higher conductivity and mechanical stability without cracks in the structure. Graphene may provide higher reaction rates with less CO poisoning and a better conductivity in parallel to higher utilization of Pt by decreasing the loading amounts. For this mentioned reasons, this thesis study is dedicated to synthesis of graphene supported Pt nanoparticles for PEM fuel cell electrodes, and characterization of synthesized materials in comparison with commercial carbon supports.

1.2. Fuel Cell Overview and a Brief History

The first illustration of a fuel cell was assembled by lawyer and scientist William Grove in 1839. Electrolysis is a process in which a voltage is applied and water decomposes to O_2 and H_2 as shown in Figure 1-1 (a). As a result of replacing the power supply with an ammeter, electrolysis is reversed and an electric current flow is observed with a simultaneous recombining of O_2 and H_2 (Figure 1-1 (b)). The chemical reaction for

reverse electrolysis is represented in Equation 1-1. This reaction can be considered similar to a burning process in which the fuel is hydrogen and electrical energy is produced eliminating heat generation.

$$2H_2 + O_2 \rightarrow 2H_2O \qquad \text{Equation 1-1}$$

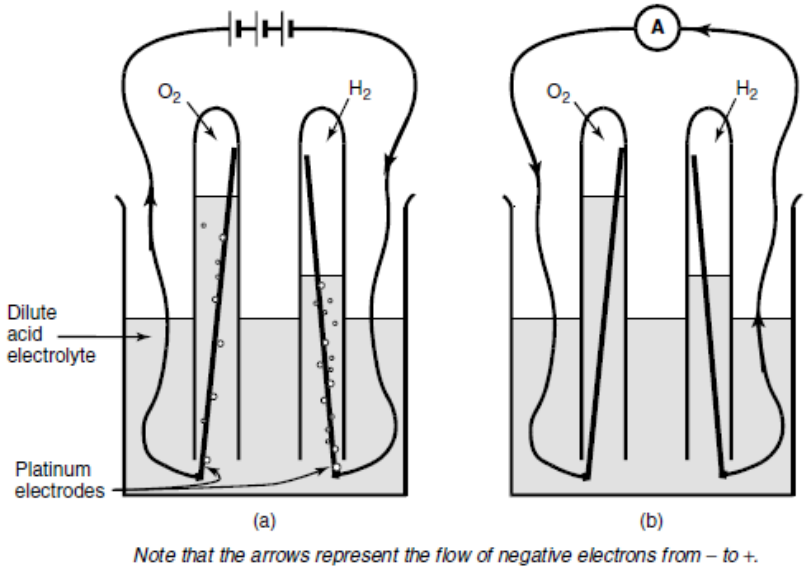

Figure 1-1 (a) Electrolysis of water (b) Reverse electrolysis of water [1]

However, the amount of electrical current produced is very limited due to the low electrode area, large distances between electrodes, gases, and electrolyte. Such limitations and the absence of a practical usage of this theory become a driving force for the evolution of fuel cells. In 1937, Francis Bacon started to work on practical fuel cells and he eventually developed a 6 kW fuel cell by the end of 1950s. The first practical fuel cell applications were in U.S Space program. General Electric produced the first PEM fuel cell and it was used in the Gemini program in the late 1960s. In the Apollo Space Program, fuel cells were used to generate electricity for life support, guidance and communication. Besides the usage in U.S Space programs, General Motors tried fuel cells for the automotive applications. Although the successful usage of fuel cell in U.S Space Program, very restricted interest arose for terrestrial applications of fuel cells until 1990s when Ballard Power Systems embodied fuel cell-powered buses. After the improvement in the production of fuel cells for transportation and stationary power generation, research and development of fuel cells have dramatically increased [2].

1.2.1. Working Principle of Fuel Cells

Fuel cell is a type of electrochemical power source that converts chemical energy into electrical energy. It differentiates from the other types of electrochemical power sources such as batteries in terms of utilization of gaseous or liquid reactants, and it is considered as an open system because of the requirement for continuous supply of reactants and elimination of products. The great attention towards fuel cells are based on both economic and environmental reasons. Higher efficiency in the utilization of natural fuels for large scale power generation can be obtained by fuel cells with an inferior amount of toxic combustion products and contaminants released to atmosphere.

A fuel cell constitutes of three main components which are anode, cathode and separator. Electrons are released at anode and conducted to external circuit resulting with oxidation whereas electrons that passed thorough external circuit are accepted by cathode electrode and reduction takes place. As the fuel cell is fed with oxygen and hydrogen gases, hydrogen oxidizes at anode side and produces electrons, then, which are conducted to the cathode side via an electrical circuit. At the time the electrons are accepted by oxygen atoms, and reduction takes place in cathode side with the product of water. The scheme for the reactions for the current generation inside fuel cells shown in Figure 1-2.

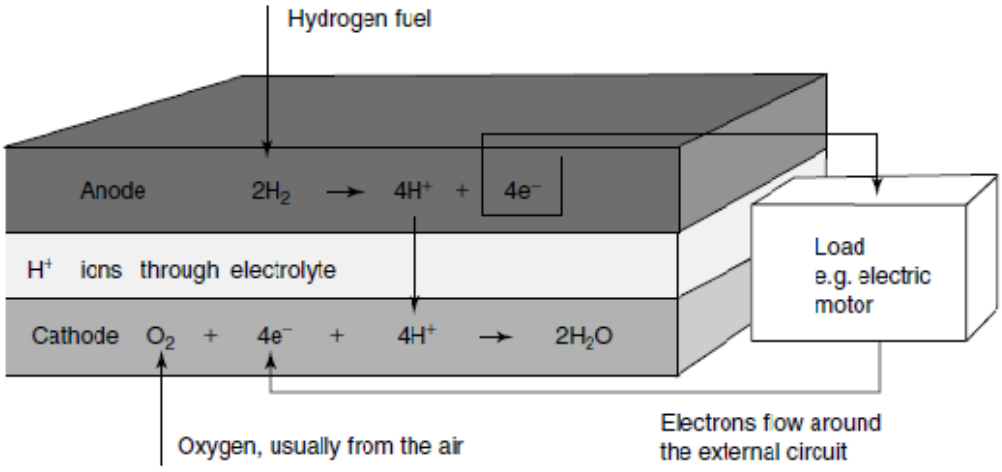

Figure 1-2. Electrode reactions and charge accumulation for an fuel cell [1].

1.2.2. Thermodynamics of Fuel Cells

Two main reactions take place inside a fuel cell and they can be seen in Figure 1-2 and Equations 1-2 and 1-3.

Anode (HOR) $$H_2 \rightarrow 2H^+ + 2e^-$$ Equation 1-2

Cathode (ORR) $$\frac{1}{2}O_2 + 2H^+ + 2e^- \rightarrow H_2O$$ Equation 1-3

Overall $$\frac{1}{2}O_2 + H_2 \rightarrow H_2O$$ Equation 1-4

The importance of reaction kinetics will be further discussed in section 1.3. The anode potential is E_a^0=0.000 V versus standard hydrogen electrode (SHE) and cathode potential is E_c^0=1.229 V versus SHE. The electromotive force of a fuel cell at equilibrium with the reactants and products is calculated to be 1.229 V.

Equation 1-4 is reported as the reaction of hydrogen combustion [3]. Enthalpy of this reaction (ΔH) can be calculated from Equation 1-5. The heat of formation of liquid water is -286 kJ.mol^{-1} and heat of formation of elements are equal to zero. ΔH of the reaction is found out to be -286 kJ.mol^{-1}. The negative sign of the enthalpy defines that this reaction is exothermic.

$$\Delta H = (\mathrm{H}_f)\mathrm{H}_2\mathrm{O} - (\mathrm{H}_f)\mathrm{H}_2 - 1/2(\mathrm{H}_f)\mathrm{O}_2$$ Equation 1-5

The change in Gibbs free energy of a reaction is very determinant to anticipate if a reaction is reversible or irreversible. The Gibbs free energy change can be calculated from the Equation 1-6. Furthermore, the change in Gibbs free energy is dependent on temperature and pressure, and Equation 1-6 can be extended to Equation 7. The calculated value of ΔG_f^0 at standard conditions for reaction seen in Equation 4 is 237.1 kJ.mol^{-1}.

$$\Delta G_f = G_{f,H2O} - G_{f,H2} - G_{f,O2}$$ Equation 1-6

$$\Delta G_f = \Delta G_f^0 - RTln\left[\frac{p_{H2}\, p_{H2}^{1/2}}{p_{H2O}}\right]$$ Equation 1-7

$$\Delta G_f = -nFE$$ Equation 1-8

This two equations are important to calculate change in Gibbs free energy of reaction, however, these are not enough to reach a conclusion about the reversibility of fuel cell reaction. The meaning of reversibility in a fuel cell is the total conversion of all the Gibbs free energy into electrical energy. Equation 1-8 demonstrates the condition for Gibbs free energy to be equal to the electrical work. F is the faraday constant, n is the number of moles of electrons that pass through the external circuit and E is the reversible cell potential.

$$\eta = \frac{\Delta G_f^0}{\Delta H_f^0} = \frac{237.1\ kj/mol}{286\ kj/mol} = 83\% \qquad \text{Equation 1-9}$$

Fuel cell efficiency is another thermodynamic aspect that should be mentioned. The efficiency for any kind of energy conversion device can be described as the ratio of energy output to energy input. The maximum theoretical value for energy efficiency of a heat engine is known as Carnot limit which is 52%. The maximum theoretical fuel cell efficiency at standard conditions is calculated as shown in Equation 1-9.

1.2.3. Types of Fuel Cells

Fuel cells are distinguished by the type of electrolyte. The summary of the fuel cell are present in the Table 1-1.

Table 1-1. Types of Fuel Cells

Type of Fuel Cell	Type of Electrolyte	Necessity for noble catalyst	Temperature (°C)	Electrical Efficiency (%)
PEMFC	Polymer solid membrane	Yes	50-100	53-60 (mobile) and 25-35 (stationary)
AFC	Aqueous alkaline	Yes	50-200	60
PAFC	Phosphoric acid	Yes	200-250	40
MCFC	Molten Carbonate	No	600-700	45-47
SOFC	Solid oxide	No	500-800	45-70

Polymer electrolyte membrane (PEM) fuel cells have a solid electrolyte where electrons are mobile. They run in a temperature range between room temperature and 100°C. Low working temperature results with slow reaction rate and in order to overcome this problem special catalysts and electrodes should be used. Also, PEM fuel cells require pure hydrogen as fuel [1].

Highly porous electrode layers with Pt catalysts were used in the alkaline fuel cells (AFC) in Apollo spacecraft. The fuel should be free from CO_2 or pure O_2 and H_2 should be used. Electrode used in AFC should be an alkaline solution such as sodium hydroxide, potassium hydroxide, sodium carbonate and potassium carbonate. The solubility and corrosiveness of alkaline solution are significant in choosing suitable electrolyte [1].

Phosphoric acid fuel cells (PAFCs) contain porous electrodes and Pt catalysts, and operate at a higher operating temperature above 200°C. Fuel that is used in this type of fuel cell can be reformed from natural gas (methane) to H_2 and CO_2. The reforming process increases the cost of the fuel cell as well as the size of it. PAFCs are very effective to produce 200 kW of electricity parallel to 200 kW of heat. This property gives them the name of "combined heat and power" systems. Although PAFCs have limitations due to their cost and size, they are greatly reliable and maintenance free systems [1].

Solid oxide fuel cells (SOFCs) operate at a temperature range in between 600°C and 1000°C so that expensive catalysts are not required to reach high reaction rates. Fuel used in SOFC might be natural gas and any further processing of fuel is not required. SOFCs intrinsically possess simplicity of the fuel cell concept. Besides these advantages, the cost of the ceramic materials which are used as electrolyte, are very high to manufacture. The SOFC systems require extra plants that include air and fuel pre-heaters. As a result of high operating temperatures, a special and more complex cooling system is necessary. Finally, the startup of the SOFC systems are not straightforward [1].

Molten Carbonate Fuel Cells (MOFCs) have higher operating temperatures as SOFCs. Unlike SOFCs, MOFCs have non-solid electrolytes at high temperatures. Enhanced reaction rates is achieved with a low-cost catalyst, Nickel, which constitutes electrical basis of the electrode. Gases such as natural gas and coal gas (H_2 and CO) can be used as fuel directly. Interestingly, MOFCs need CO_2 in the air to work. The nature of the electrolyte, which contains a hot, corrosive mixture of lithium, potassium and sodium

carbonates, constitutes a drawback by eliminating the simplicity of the fuel cell system [1].

1.2.4. Advantages of PEM Fuel Cells

PEM fuel cells are differentiated from other types of fuel cells containing a semisolid electrode composed of a polymer backbone with acidic functional groups attached to this backbone. The required temperatures to activate the catalyst in the PEM fuel cells are relatively low and this feature makes their usage more appealing in the scope of applications such as transportation, household-based distributed power, and portable power devices. PEM fuel cells provide a high power density and quick start-up at relatively low temperatures [3]. Membrane electrode assembly (MEA) is the most significant part of a PEM fuel cell. MEA consists of two porous conductive electrodes which are separated by a polymer electrolyte membrane. The electrode layers are mostly carbon cloth or carbon fiber paper which allows the permeation of gases. These layers hold the catalyst particles which are generally supported on carbon materials. An illustration of MEA can be found in Figure 1-3. Since higher efficiencies are strongly related with the catalyst surface, MEAs are fabricated in a flat shape to enhance the larger surface area of the catalyst. The thin and flat morphology of MEAs actualize compact fuel cells.

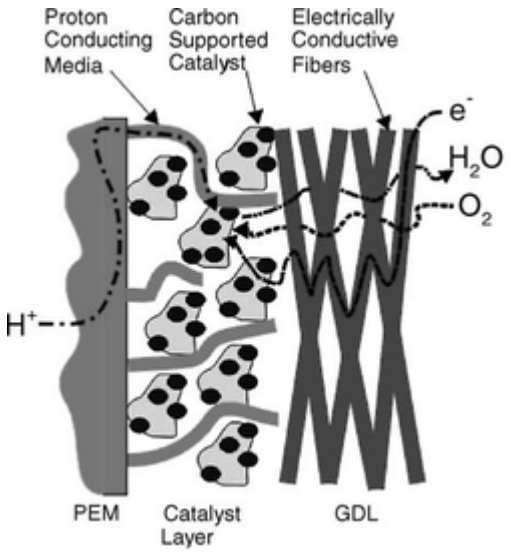

Figure 1-3. Illustration of membrane electrode assembly (MEA) [4]

In addition, fuel cells are electrochemical power plants that accomplish conversion of chemical energy into electrical energy efficiently without emission of pollutant gases [5]. A PEM fuel cell does not contain corrosive fluid hazards such as the corrosive electrolytes used in MCFCs, and as a result it can work in any orientation. This property enlarges the extent of fuel cell usage to vehicles industry and portable applications.

1.3. Importance of Catalyst Layer

As it is explained briefly in the section 1.2.4, MEA includes two electrode layers, which are called cathode and anode separated by a polymer electrolyte membrane. These electrode layers are fabricated by coating of carbon supported metal nanoparticles on gas diffusion layers (GDLs). Fabricated electrodes are also known as catalyst layer as a result of metal catalyst incorporation. Catalyst layer functions as the main place for electrochemical reactions. The catalyst nanoparticles are the active sites where all the reactions takes place on their surface, and in the absence of catalyst nanoparticles, the required energy to break bonds of fuel molecules at low operating temperatures cannot be reached. Catalyst layer basically consists of metal catalyst, carbon support and ion conducting polymer electrolyte (ionomer). Anode catalyst layer has a negative potential and carries electrons that are produced in hydrogen oxidation reaction (HOR) to external circuit. Cathode catalyst layer is the electrode with a positive potential, and accepts electrons back from the external circuit and water is produced by recombination of electrons with hydrogen ions and oxygen. The anode and cathode reactions are demonstrated in the Equation 1-2 and 1-3. The overall reaction is represented in Equation 1-4. The cathode catalysts layer in PEM fuel cells contain mostly Pt group metal/alloy nanoparticle supported on a carbon support to enhance the rates of ORRs [6]. Pt is also used in anode catalyst layer even though there is an immense potential differences between ORR and HOR reaction rates.

The design of catalyst layer should be done very meticulously in order to obtain high reaction rates from anode and cathode reactions, and to optimize the amount of catalyst for attaining the essential levels of power output. A catalyst layer should satisfy many objectives to perform efficiently. A three phase interface where electrode, electrolyte and

reactant gases interact has to be as large as possible to provide sufficient area for electrochemical reactions (Figure 1-4).

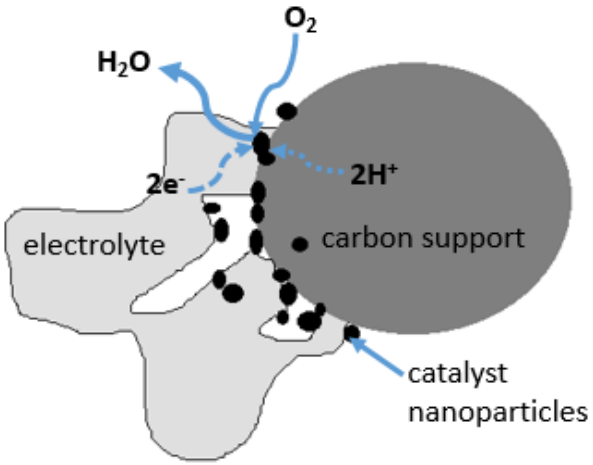

Figure 1-4. Three phase interface in catalyst layer

Moreover, catalyst layer has to allow transport of protons efficiently. Transport of reactant and product gases as well as removal of water product out of cell reactions has to persist without any interruption. Additionally, electronic current between reaction sites inside catalyst layer and current collector should flow continuously.

1.4. Catalyst Support Materials

The distinctive elements of catalyst support are synthetic composition of materials used, surface area, stability and durability. The basic role of catalyst support is to maintain a catalytically active phase in a highly dispersed state. A high value of surface area and developed porosity help to achieve large metal dispersion. The stability of support materials to the aggressive fuel cell environment is a significant achievement. Carbon based materials have been predominantly used as catalyst supports in PEM fuel cell electrodes. Graphitic structures in carbon supports were reported as important elements to enhance better resistance towards corrosion. However, as corrosion resistance increases with highly graphitized structures of carbon support, fuel cell performance decreases. The performance of fuel cell, electrocatalysts stability and membrane degradation is strongly affected by the morphology, and the physical and chemical characteristics of these carbon supports [6].

The affinity of carbon supports to metal nanoparticles is also very significant to attain higher performances. Carbon supports are crucial in the dispersion of Pt nanoparticles in order to enhance a higher active Pt surface area. The properties of carbon supports may have effects on electrical conductivity, corrosion resistance, surface properties and cost.

At a given catalyst loading, the performance of a catalytic layer depends on the distribution of catalyst and electrolyte chains, and the microstructure of a layer. Pore structure is strongly related to gas transport through the catalytic layer. Easy transport and access through all of the catalyst particles increases the interaction between the gases and catalyst with a positive effect on cell performance [7]. Carbon support materials possess an excellent electron conductivity, corrosion resistance, and surface properties as well as providing cost advantage for integration of fuel cells into market. Also, carbon supports significantly contribute in obtaining expanded active Pt surface area by enabling a better dispersion of small Pt particles [8].

CBs are the main carbon materials for catalyst support. Their conductivity range from 0.1 to 10 $S.cm^{-1}$ [9]. Vulcan®XC-72 (BET specific surface area of 250 $m^2.g^{-1}$) is the most regularly used carbon support which was primarily utilized for PAFC catalysts but also applicable to PEMFC as catalyst supports [5]. The conductivity of Vulcan®XC-72 was reported to be 4-7.4 $S.cm^{-1}$ at different packing pressures [10]. Studies showed that the surface area of CBs affects the particle size of Pt nanoparticles in an inversely proportional manner, and the method for the catalyst preparation has a tremendous effect on the surface area and catalytic activity of Pt/C [11]. As CBs are the mainstream materials for PEM fuel cell catalyst layers, recent studies have focused on problems with CBs and tried to enhance improved activities with alternative preparation methods [11-13]. Another approach to develop catalyst activities is based on replacing CBs with conventional carbon materials.

Carbon nanotubes (CNTs) have attracted a great amount of attention due to their high mechanical and electrical properties [14]. They have also became good candidates for catalyst support materials for direct methanol fuel cells (DMFC). Wenzhen Li *et al.* reported the utilization of CNT with a BET surface area of 42 $m^2.g^{-1}$ as catalyst support for Pt nanoparticles [15]. The idea to improve ORR kinetics of cathode materials has developed the approach towards the utilization of novel carbon materials as catalyst supports. Articles have supported this approach by showing better ORR activity and

higher performance of DMFC in comparison to commercial carbons [15]. Different synthesis methods were also reported in which MWCNT was used as catalyst supports for Pt and the surface modification of MWCNT was examined. CNT utilization in cathode and its ORR activity was investigated [16, 17]. The importance of the synthesis methods has attracted a great amount of attention due to their effect on particle size, dispersion and cost reduction. CNT and other carbon based materials such as carbon nanofibers (CNF) are functioned as catalyst support to increase Pt utilization by reducing the Pt loading and to enhance a better catalytic performance [18]. In the case of Pt deposition on CNT, CNT surface was treated with aggressive reagents in order to create surface groups such as hydroxyl (–OH), carboxyl (–COOH) and carbonyl (–C=O) for a better Pt adsorption on CNT [19].

CNTs have been considered to be more corrosion resistant than CBs; however, the cost of CNT production stands as a barrier for commercialization. In addition to CNT and conventional CBs, mesoporous carbons (MPCs) containing monodispersed mesopores (pore size >2 nm) were considered as possible candidates for catalyst supports and ORR kinetics of MPCs were investigated for PEM fuel cell applications [20, 21]. One drawback of MPCs is that they show similar corrosion behavior to CBs due to similarities in the graphitization rates. Further improvements were accomplished in order to solve this problem by increasing the graphitization of MPCs with hard template synthesis at high temperatures, and materials were reported as having better corrosion resistance whereas they showed catalyst loss [22] . Studies about the effect of using MPCs as catalyst supports on catalytic activity have been conducted and the results were showed that MPCs were not effective in improving catalytic activity of MEAs, whereas they were considered to improve the mass transport properties of the catalyst layer [23].

It is already mentioned that CBs are not resistant to corrosion due to excess electrochemical oxidation. Additionally, carbon is impermeable to the gases and liquids and this feature of carbon leads to limited catalyst performance, low catalyst utilization and reduced cell performance. An ionomer (Nafion® solution) functioning as a binder for catalyst support and catalysts particles should be introduced to the catalyst layer. The idea to replace both carbon and Nafion® ionemer brought the attention to an alternative group of materials which are conjugated heterocyclic conducting polymers. This group of materials captivate interest due to their unique metallic/semiconductor characteristics and their potential use in areas such as electronics, biosensors and actuators, electrochemistry

and electrocatalysis [24]. Among conducting polymers, polypyrrole (PPy) can be distinguished as a prosperous catalyst support material with its good environmental stability, facile synthesis, and high conductivity [25]. The presence of connected pyrrole rings in the structure gives rise to the mobilization of electrons and facilitates the electrical conductivity of PPy. PPy can be synthesized via chemical or electrochemical polymerization which increase the control chance of the properties of synthesized nanoparticles. PPy provides a good adhesion between Nafion membrane and Pt nanoparticles, and Pt utilization can be improved in the presence of PPy [25]. Polyaniline (PANI) is another conducting polymer that has been investigated as possible catalyst support materials owing to high accessible surface area, good electronic conductivity, stability over a wide potential range. PANI nanofibers can easily synthesized by a interfacial polymerization and a subsequent process can be conducted to decorate Pt nanoparticles on PANI nanofibers [26]. The usage of conducting polymers as catalysts supports for Pt nanoparticles in fuel cells demonstrated comparable results with Pt/C catalyst. However, there should be further investigations for stable and reproducible performance [27].

1.5. Graphene as a Support Material in PEM Fuel Cells

Graphene is a single atom thick material with a very good hexagonal lattice structure. Graphene has become a very hot topic after the study of Novoselov *et al.* [28] in which they obtained very few graphene layers by the mechanical cleavage of graphite, and they were rewarded with the Nobel prize in physics in 2010. After that advancement, many scientists have been working on graphene in various areas such as chemistry, physics, electronics and so forth. The properties of graphene such as conductivity, high surface area, thermal and mechanical stability are very appealing for practical application.

The above mentioned properties of graphene distinguishes from the other carbon supports and have been considered to be a new candidate for catalyst supports in low temperature fuel cells. The roles of graphene in fuel cells were reviewed by Hur and Park [29]. The uniformity in the distribution of nano-sized particles, and the increased enhancement between defect sides of graphene and nanoparticles have been highlighted as two

significant conditions that might likely be satisfied by graphene for better catalytic activity and fast charge transfer.

The quality and preparation method of graphene have also a great impact on the efficiency of chemical reactions that are taking place in the catalyst layer. Graphene can be prepared by top-down or bottom-up methods, and the preparation method strongly affects the structural properties of graphene. Chemically converted graphene, which is obtained by oxidation of graphite, has many defect sides whereas chemical vapor deposition (CVD) method can provide one layer graphene without defects. Computational studies about the interaction of Pt nanoclusters with point defects of graphene revealed that on the defect sides strong Pt–carbon bonds are formed and showed improved tolerance toward CO poisoning [30]. Graphene sheets prepared by thermal expansion of graphene oxide (GO) have been selected as promising support materials for electrocatalysts due to higher electrochemical surface area (ECSA) and better oxygen reduction activity [31]. Graphene nanoplatelets (GNPs) consisting of 10 or more layers of graphene sheets were reported to have characteristics of both single-layer graphene and highly ordered graphitic carbon [32]. The integration of graphene into the catalyst layer have been accomplished via both chemical and electrochemical methods which will be further explain in section 1.6.

1.5.1. Graphene Synthesis

Graphene has been synthesized by various methods such as mechanical cleavage of graphite [33], CVD [34], chemical exfoliation methods. Even though mechanical cleavage method is an effective method to obtain defect free graphene layers, it is not suitable for large scale production and that constitutes a drawback for industrial applications. CVD method is a bottom-up method to nucleate and grow single layer of graphene on top of transition metal surfaces after decomposition of hydrocarbons such as ethylene, methane, or acetylene at high temperatures. The problem with CVD method is that the transmission of graphene to a rigid, insulating substrate for practical application.

Chemical exfoliation of graphene is a top-down method which utilizes graphite containing many stacked graphene layers and aims to isolate single or few layered graphene. The isolation of graphene has been achieved by various approaches. The most common approach is the chemical oxidization of graphite layers which enables separation

of graphene layers by inserting functionalities in between them. The chemical oxidation of graphite is carried out using potassium chlorate and fuming nitric acid in Brodie's method [35]. Concentrated sulfuric or nitric acid and chlorate is used for graphite oxidation in Staudenmaier method [36] and Hummer's method oxidizes graphite with potassium permanganate and sodium nitrate in concentrated sulfuric acid [37]. All of these chemical procedures are highly effective in oxidizing of graphite layers, however, the generation of toxic gases such as NO_2, N_2O_4, and/or ClO_2 creates practical problems. Consequent studies in literature mostly have preferred to use Hummer's method or various modifications of Hummer's method by changing the ratio of reactants or the reaction conditions in order to have a milder reaction medium. A very recent Hummer's method is reported by Marcano *et al.* in the name of "Improved Synthesis of Graphite Oxide" [38]. Instead of using highly toxic reactants, oxidation is achieved by a mixture of concentrated sulfuric acid and phosphoric acid. Resulting GO is compared with the GO produced by Hummer's method and a modified Hummer's method. Improved GO is underlined to have higher amount of oxygen containing groups and fewer defects on basal plane compared to other two methods. The conductivity of improved GO is also measured, however, none of the GO samples provide effective conductivity values. The presence of oxygen containing functionalities composes interruption areas for electronic conduction. Removal of these surface functionalities by hydrazine reduction or thermal treatment is noted to be effective in obtaining a higher conductivity.

A general route has been mostly followed in the synthesis of graphene sheets. Oxidation of graphite provides an enlargement in the interlayer spacing of graphite and thermal exfoliation or ultrasonication might boast the degree of sheet separation. A consecutive reduction of surface groups has to be performed in order to reach optimum properties in conductivity. The conditions of reduction process has a tremendous effect on the quality of final graphene product because excessive removal of functionalities should be accomplished while preventing graphene layers from restacking. Chemical reduction of GO is reported to be attained by hydrazine hydrate [38, 39], hydroquinone [40, 41], sodium borohydride [42], Fe powder [43]. Instead of a chemical reduction or in combination with a chemical process, thermal treatment of GO surfaces are used in order to obtain graphene sheets [44, 45]. A simple and combined method utilizing thermal treatment and ultrasonic irradiation is also worth to mentioned [46]. Electrochemical reduction of GO is also reported in the literature in small scale. GO dispersion is applied

onto a glassy carbon electrode and immersed into Na_2SO_4 solution, and electrochemical reduction is achieved during extended cyclic voltammetry [42, 47].

1.6. Catalyst Deposition Methods on Graphene Supports

Electroless deposition enables the reduction of metal ions which are dispersed in an aqueous solution in the presence of a chemical reducing agent. This process aims to deposit metal nanoparticles on a carbon support without using electrical energy. The integration of metal platinum ions into catalyst layers is extensively enhanced by a wide range of electroless deposition techniques. The reduction of Pt cations into Pt metal can be accomplished via chemical reducing agents, thermal treatment or a combination of different techniques.

Pt deposition on functionalized graphene sheets (FGSs) with H_2 gas at 300°C were reported by Liu *et al.* [31]. Although they did not investigated fuel cell performance of electrocatalysts, oxygen reduction activity with an improved ECSA was accepted as promising compared to commercial catalyst E-TEK and the durability of Pt/FGS was found out to be more durable than commercial one.

Chemical reducing agents are widely used to obtain reduced nanoparticles deposit on carbon supports. Sodium borohydride ($NaBH_4$) is one of the most common reducing agents utilized in reduction process of metal cations. In an article published by Xin *et al.*, the reduction of GO and Pt cations in solution with pH adjusted to 10 were concurrently completed by $NaBH_4$ treatment [48]. Products of this treatment (Pt/G) were dried with lyophilization and further annealed at 300°C under N_2 atmosphere. Methanol oxidation on Pt/G were tested and they demonstrated higher catalytic activity than Pt/C. The authors were remarked that the distinctive interaction between Pt and graphene might be the reason for this improvement parallel to obtaining larger ECSA of Pt/G which can perform as Pt activity sites for chemisorption of methanol. In another study, different platinum precursors were dissolved in deionized water in the presence of GO as catalyst support and polyvinylpyrrolidone (PVP) as stabilizer [49]. Immediate color change was observe when freshly prepared $NaBH_4$ solution was added to Pt/GO/PVP suspension and this color change was attributed to successful reduction of GO. The physical and electrochemical examination of products of this study were done, and superior activities

were obtained for the electrooxidation of methanol and ethanol in acid media. A similar stabilizer usage for Pt nanoparticles during the reduction process were explored in other studies. One of this studies were used a cationic polyelectrolyte, poly(diallyldimethylammonium chloride) (PDDA) in order to stabilize Pt nanoparticles by avoiding their agglomeration in the solution [50]. The stabilization of Pt nanoparticle prior to $NaBH_4$ reduction was achieved and Pt nanoparticles were decorated on CB support. The presence of PDDA was pointed out to be significant in the improvement of both oxygen reduction activity and electrocatalysts durability. The same approach also employed in the preparation of Pt nanoparticles on top of graphene supports [51]. Another study attributed PDDA to functionalize GO and proposed a subsequent Pt reduction on PDDA/GO supports with $NaBH_4$ [52]. Although a stabilizer assists to reach a more steady dispersion, on the other hand, its molecules might be placed in catalytic sites of electrocatalysts and that would result in a lower the catalytic performance [53]. A recent study proposed a colloidal method without the use of any stabilizer in the reduction process of Pt nanoparticles [54]. Colloidal platinum oxides were prepared with the addition of NaOH followed by vortex mixing, and they kept undisturbed at room temperature. The colloidal platinum oxides was effectively mixed with partially reduced GO. $NaBH_4$ was added to the final solution under continuous stirring and nanoparticles obtained at the end of centrifuging. The quality of colloids was very important for effective reduction so that the influence of solution pH in colloid preparation step was further investigated. Electrocatalytic oxidation toward formic acid and ethanol of the final products were found out to be 3 times higher than the commercial Pt/C catalysts.

Ascorbic acid was noted as an effective reagent in reduction due to its strong reducibility at high temperatures [55]. Ascorbic acid was added to GO suspension under continuous stirring. After that, chloroplatinic acid (H_2PtCl_6) was added, and the solution was transferred into a Teflon beaker in order to increase the temperature up to 160°C. The catalytic activities of Pt/G nanoparticles were investigated via methanol oxidation and Pt/G were regarded as having a higher catalytic performance compared to only Pt nanoparticles toward methanol oxidation.

Many different reducing agents have been functioned in nanoparticle synthesis for fuel cell application. The effectiveness, activation conditions and hazardous rates of reducing agents are crucial. A very common reducing agent $NaBH_4$ was indicated as highly hazardous, and researchers observed inhomogeneous distribution of Pt nanoparticles on

GO supports when $NaBH_4$ was used as reducing agent [52]. Polyol process have been considered to be milder and environmental friendly. Ajayan *et al.* stated the usage of ethylene glycol as both reductive and dispersive agent [56]. The dispersion of GO and H_2PtCl_6 in water-ethylene glycol mixture was ultrasonically treated and successive reduction was carried out at 120°C under continuous stirring. The similar process was repeated in many other studies in order to compare with different techniques and to have a detailed insight about the reaction parameters [57-60]. Further, the dispersion of Pt nanoparticles was aimed to be improved with the addition of PDDA while utilizing polyol method in the reduction of Pt nanoparticles [61]. GO was grafted with PDDA by addition of GO powder into PDDA solution. The pH of the solution was adjusted to 2. After GO/PDDA particles were prepared, they combined with H_2PtCl_6 solution in ethylene glycol followed by pH adjustment to 10. The reduction of resulting solution was completed with microwave heating. In a similar study, the PDDA functionalized GO was prepared in EG and then transferred into H_2PtCl_6 solution followed by a microwave heating process [62]. The pH adjustment was involved just before centrifuging step. In another study, PDDA was also adsorbed on the hydrophobic surface of GNPs by simply adding PDDA solution into GNPs dispersion [32]. A better attachment of PDDA onto GNP was achieved by ultrasonication, and KNO_3 was added to obtain a stronger attraction between them. A similar Pt deposition technique to previous mentioned procedures was utilized to produce Pt decoration onto PDDA/GNP.

1.6.1. Electrodeposition of Catalyst Particles

Electrodeposition is a process in which electrical current is employed to reduce dissolved metal cations in order to obtain a coherent metal coating within the electrode layer. The electrodeposition method have drawn attention due to efficient Pt utilization by achieving the deposition of Pt particles at the most efficient contact zones with both ionic and electronic accessibility on the electrode layer [63, 64]. The first patent detailed electrodeposition method and reported the fabrication of a non-catalyzed carbon electrode with Pt loadings as low as 0.05 $mg.cm^{-2}$ [65].

The parameters that directly influence electrodeposition performance reported as current density, pulse conditions, duty cycle, and electrode surface condition [66]. Pulse

electrodeposition was regarded as a preferable method over DC electrodeposition due to controlled particle size, stronger adhesion and uniform electrodeposition in the study of Choi *et al.*. This superiority was associated with the fact that only one variable, current density, alters the performance of DC electrodeposition whereas pulse electrodeposition provides a better control over performance with the help of three variables which are t_{on} (time-on), t_{off} (time-off) and i_p peak current density. This study further reported that catalysts with smaller particle size would be obtained via pulse electrodeposition method.

Electrodeposition method was improved, and the utilization of a Pt plating bath for direct deposition of Pt particles on the carbon blank electrode was reported by Kim *et al.* in 2004 [67]. In this improved method, the blank carbon electrode was coupled with a copper plate and this copper plate functioned as a current collector. The anode was a Pt gauze. The pulse wave and the deposition current density was regulated with a pulse generator. The authors emphasized the possibility to enhance a Pt/C ratio up to 75 wt% close to the electrode surface. In a consequent article of Kim *et al.*, pulse electrodeposition parameters were examined to enhance a better performance from the catalyst layer [68]. Therefore, the results of this studies are proclaimed that pulse electrodeposition is a very strong candidate to replace the traditional MEA preparation methods with the benefit of catalyst cost reduction and increased PEMFC efficiency.

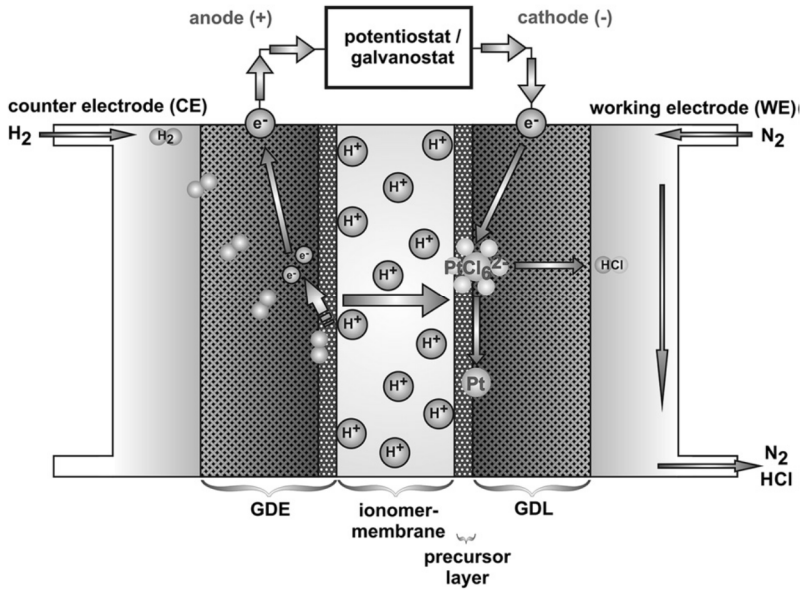

Figure 1-5. Design of an electrodeposition cell comprising a Hydrogen Depolarized Anode (HDA) [69]

The electrodeposition method have been further adopted to reduce Pt nanoparticles onto graphene supports. The electrochemical reduction of Pt was attained by potentiostatic electrodeposition using a hydrogen depolarized anode (HDA) on graphene layers [57]. The theory of HDA method was explained accurately in a previous article by Mitzel *et al*., and a scheme of this method can be seen in the Figure 1-5 [69]. The benefit of this method in which the ionomer is only used as ion conducting phase in the electrodeposition process is the absence of liquid phases on that electrode. This property provides the necessary contact of the build catalyst particles to the ion conducting phase in the fuel cell while it eliminates the precursor diffusion. MEAs were prepared by coating graphene ink containing Pt cations on GDLs and dried subsequently, and then directly integrated to the potentiostat as cathode. The results of the electrochemical deposition method with the HDA revealed to be advantageous in terms of enabling low amount of catalyst loading by providing a uniform distribution of the platinum particles on the supporting material. The electrochemical reduction method contributes to the alignment of platinum catalysts at the three phase boundaries (TPB).

1.7. Hybrid materials as Catalyst Supports in PEM fuel cells

In the process of membrane electrode assembly (MEA) fabrication, graphene sheets are inclined to stack to form graphite as a result of its 2D nature and strong van der Waals interactions. This behavior of graphene sheets leads to a decrease in the surface area of graphene and inevitably to a lower fuel cell performance. One method for better Pt utilization and electrocatalytic activity is to increase the amount of ionomer used in MEA fabrication. However, high amount of ionomer can be a drawback by decreasing the conductivity and creating mass transport limitations. There are other proposed methods in the literature such as introducing spacer particles in between graphene sheets resulting with a larger interface. The crucial point about spacer introduction to the structure of graphene is to protect the conductive network of graphene sheets. CB is one of the candidates to intercalate graphene sheets by virtue of its high electrical conductivity and cheap price. In literature, the use of CB as spacer for graphene was first reported by Yan *et al*. [70]. The integration of CB in between graphene nanosheets (GNSs) was underlined to be effective in decreasing the agglomeration of GNSs while minimizing the diffusion path in double layer capacitance. GNS/CB hybrids were prepared by a chemical reduction

with hydrazine at higher temperatures after exfoliation of hybrids in ultrasonic bath. Another study utilized a similar method in preparation of r-GO/CB hybrid dispersion to be used in formation of r-GO/CB hybrid gel films by a simple vacuum filtration [71]. However, these two studies did not give information about the application of this hybrids as catalyst supports in fuel cell electrodes. The study of Park *et al.* provides an insight about the effect of spacer in the electrochemical features of the cathode in PEM fuel cells [72]. In this study, Pt nanoparticles firstly deposited on TRGO via polyol method, and the resulting powder was combined with CB in Nafion® solution, DI water and methanol in order to be used as catalyst ink. The prepared catalyst ink was used to fabricate electrodes. The analysis of ECSA and double-layer capacitance of electrodes containing different CB amount revealed that Pt/G with CB spacer had a higher ECSA value in comparison with the ECSA of plain Pt/G.

The above mentioned hybrid structures with CB are mostly prepared to observe intercalation of graphene sheets and lower amount of agglomeration without decreasing conductivity. Apart from CB usage, CNTs were also mentioned in the literature as an intercalating agent. Additionally, CNTs can provide mechanical stability due to their orientations in hybrid structures [73]. As the agglomeration of graphene sheets increases, the presence of graphitic structures leads to a dramatic decrease in the stability of graphene. The loss in mechanical strength can compensate with the flexible and robust properties of CNTs. With this integrated structure of graphene and CNTs, the fast charge transport pathways in polycrystalline graphene sheets can be enhanced as a result of lower sheet resistance. A study published by Cheng *et al.* promoted single-walled carbon nanotubes (SWCNTs) which have high surface area (407 $m^2.g^{-1}$) and high conductivity (100 $S.cm^{-1}$) as conductive additive, spacer, and binder in the G/CNT supercapacitors [74]. Besides the applications of G/CNT hybrids on supercapacitors, very limited number of studies were reported on G/CNTs on fuel cell applications. Jha *et al.* published research on G/MWCNT as catalysts support for Pt and PtRu electrocatalysts [75]. Thermally reduced and functionalized graphene were combined with MWCNT in deionized water and dispersed via ultrasonication. H_2PtCl_6 solution was added to the resulting mixture and chemical reduction by $NaBH_4$ was conducted. The physical and electrochemical analysis of resulting products proved the successful reduction of Pt on G/MWCNT supports. MEAs of this hybrid materials were fabricated and further tested for methanol oxidation and ORR. The outstanding results of prepared MEAs with high power densities

were recorded and the improvement was correlated with the improved accessibility of reactant gases to catalyst particles.

1.8. Objectives

The studies replacing CB supports with graphene derivatives demonstrated promising results for fuel cell applications. The superiority of graphene with enhanced stability and CO tolerance toward fuel cell applications were reported in various articles as mentioned in the literature review above. Additionally, graphene provides a large area for the integration of Pt and assists to create a conductive network for electronic applications. The deposition methods gain a great importance to incorporate Pt on graphene support with high Pt utilization and low particle size. The proposed methods for Pt deposition on carbon supports have been applied for graphene supports and the results of the studies were mostly compared with commercial Pt/C catalysts. However, the detailed comparison between Pt deposition methods on graphene supports have not been done. The reaction conditions such as temperature, time, and the ratio of reactants, the amount and the type of reducing agents should be controlled and kept constant while making a reliable comparison in between type of catalyst supports and reduction methods. According to the literature review, the most promising methods were determined and the interesting derivatives of graphene were chosen as catalysts supports to be investigated. In the light of pre-investigation, this thesis attempts to give a perception in the area of Pt deposition (EG, $NaBH_4$ and ascorbic acid) methods on several graphene supports (GNP, GO and TRGO) in comparison with each other as well as commercial Pt/C catalysts. In addition, different Pt precursors (K_2PtCl_4, H_2PtCl_6) were compared after the comparison in reduction methods were concluded. After the physical and electrochemical characterization of products, electrode layers were prepared with the most promising catalyst and the electrodes and tested in-situ fuel cell conditions. The theoretical benefits of graphene supports are intended to be supported with experimental findings.

As a future work, an alternative aspiration was also determined. The remarkable properties of hybrid structures were mentioned quite promising for fuel cell applications and graphene in corporation with other carbon supports would even result with higher fuel cell performances. With the guidance of concluded study about Pt deposition

methods and graphene supports, the most prosperous method and graphene derivative will be selected and utilized in preparation of hybrid structures as catalyst supports materials.

2. EXPERIMENTAL

2.1. Materials

The graphite flakes used in graphene oxide synthesis were obtained from Sigma Aldrich. Potassium permanganate ($KMnO_4$), sulfuric acid (H_2SO_4), phosphoric acid (H_3PO_4), peroxide (H_2O_2), hydrochloride (HCl), chloroplatinic acid (H_2PtCl_6), potassium tetrachloroplatinate (K_2PtCl_4), L-Ascorbic acid ($C_6H_8O_6$), ethylene glycol ($HOCH_2CH_2OH$), sodium borohydride ($NaBH_4$), isopropyl alcohol (C_3H_8O), perchloric acid ($HClO_4$), Nafion® (5 wt. % in alcohol) were also purchased from Sigma-Aldrich. Vulcan®XC-72, Pt / Vulcan®XC-72, Toray carbon paper (THP-H-030,110 μm) and Nafion® PFSA NR211 membrane were supplied from Fuel Cell Earth LCC, and graphene nanoplatelets (GNP) were purchased from XG Sciences. All chemicals were used without further purification.

2.2. Methods

2.2.1. Graphene Oxide Synthesis

GO was synthesized by improved Hummers method [38]. Graphite flakes were weighed and placed into a round bottom flask. After addition of $KMnO_4$ with a known ratio on top of graphite flakes, solids were magnetically stirred. Then, acid mixture of H_2SO_4:H_3PO_4 was slowly added onto the solid mixture of graphite and $KMnO_4$ inside an ice bath. Gas evolution which is the indication of oxidation was started immediately. The reaction flask was placed into the oil bath at 50°C just after the gas evolution stopped and left under reflux in overnight stirring. Transition of the reaction color from purple to yellow-brown after 24 h was enhanced. In order to ensure that the oxidation of graphite was completely accomplished, H_2O_2 was added as a further utilized as an oxidizing agent. The resulting solution was centrifuged and washed with water, diluted HCl solution and ethanol several times. The final product was dried in oven at 70°C.

2.2.2. Thermal Reduction of Graphene Oxide

The reduction of functional surface groups on GO was processed via heating up to higher temperatures. Thermal treatment contributed in expansion of interlayer distance between the sheets. The GO nanoparticles were put into a quartz tube and placed into the Protherm ASP 11/300/400 furnace. The thermal reduction was conducted under the Argon atmosphere at 1000°C for 10 minutes to obtain TRGO.

2.2.3. Synthesis of Platinum/GO and Platinum/GNP

Pt nanoparticles were impregnated on commercial GNP, synthesized GO and TRGO by various chemical reduction processes. In case of GNP, prior to the deposition of Pt nanoparticles, a mild and environmentally friendly citric acid was used to increase the anchoring surface groups on GNP. Consequently, the most common chemical reduction agents in literature were chosen and implemented for GNP, GO and TRGO. Table 2-1 summarizes the utilized graphene supports and reduction methods. The impregnation methods are explained in details on below.

Table 2-1. Catalyst supports and the methods that were used to reduced Pt precursor (H_2PtCl_6)

Sample Name	**Functionalization**	**Reducing Agent**		
	Citric acid	**$NaBH_4$**	**Ascorbic Acid**	**Ethylene Glycol**
GNP	+	+	+	+
GO	-	+	+	+
TRGO	-	-	-	+
Vulcan®XC-72	-	-	-	+

2.2.3.1. Ascorbic Acid Reduction

Both GNP and GO (0.5 $mg.mL^{-1}$) were ultrasonicated with DI water for 30 minutes to have homogenous dispersions. Afterwards, 45 mg ascorbic acid and H_2PtCl_6 (0.25 $mg.mL^{-1}$) were added to the graphene dispersion. The reaction continued at 160°C for 1 h. Finally, the resultant mixture was centrifuged, the solid was washed with DI water and ethanol several times, and subsequently dried in the oven at 60°C.

2.2.3.2. Sodium Borohydride Reduction

Both GNP and GO (0.5 $mg.mL^{-1}$) were ultrasonicated with DI water for 30 minutes. Then, the solid dispersion and H_2PtCl_6 was mixed with ratio of 2:1 (w:w) respectively. Obtained solution was ultrasonicated for 30 minutes. Afterwards, pH was adjusted to be below 2 in the presence of HCl. This solution was left undisturbed for 2 h to be stabilized. Finally, 50 mM $NaBH_4$ solution was added drop wise until all the H_2PtCl_6 was reduced to metallic Pt. Resultant solution was centrifuged 3 times with 0.1 M HCl and the final solid product was dried in the oven at 60°C.

2.2.3.3. Ethylene Glycol Reduction

Separated homogenous dispersions of GNP, GO, and TRGO (0.5 $mg.mL^{-1}$) in DI water subsequent to mixing with H_2PtCl_6 (0.25 $mg.mL^{-1}$) were ultrasonicated for 30 minutes. The resulting mixture was added to reaction flask, then 5:4 (w:w) ratio of GO, ethylene glycol and heated up to 150°C under continuous stirring for 12 h. To end the reaction, the temperature was left to go down to room temperature and the solid products were collected by centrifuging followed by drying process at 60°C inside the vacuum oven.

2.2.3.4. Citric Acid Functionalization

GNPs (1 $mg.mL^{-1}$) were ultrasonicated with DI water for 30 minutes. Then, known amount of citric acid was added to the dispersion for overnight stirring. Solution pH was adjusted to be below 2 in the presence of HCl. The resulting mixture filtered, washed with deionized water and heat treated at 300 °C for 30 minutes. H_2PtCl_6 was added into the dispersion of functionalized GNP in 2:1 (w:w) ratio respectively The resulting mixture was again ultrasonicated for 30 minutes. For chemical reduction $NaBH_4$ was added to GNP/H_2PtCl_6 dispersion by dropwise under continuous stirring and refluxed at 90 ° C with for 3 h. Finally, solid products were collected by centrifuging and then, dried at 60°C inside the vacuum oven.

2.2.4. Comparison of Platinum Precursors

Ethylene glycol reduction was chosen as the most promising chemical reduction method as discussed in further sections to impregnate the Pt nanoparticles both on GNP and GO. In the previous experimental sections, H_2PtCl_6 salt was performed as catalyst metal precursor. The effect of Pt precursor was also aimed to be discussed, and the other common platinum precursor in chemical reduction processes, K_2PtCl_4 was also employed onto the GO/TRGO in order to compare with H_2PtCl_6 (Table 2-2).

Table 2-2. The effect of platinum precursor change in the reduction processes

Pt Support	**H_2PtCl_6**	**K_2PtCl_4**
GO	+	+
TRGO	+	+
Vulcan®XC-72	+	+

2.3. Characterization Methods

2.3.1. Material Characterization

2.3.1.1. X-ray Diffraction (XRD)

X-ray diffraction (XRD) is a physical characterization method to gather information about crystalline structures of materials. X-ray diffractometer utilizes X-rays that are generated at the end of an acceleration process of electron beams to be focused onto a pure metal material. A diffractometer assembly controls the positioning of the generated beam in coordination with the position of the specimen and the X-ray detector [76].

The requirement for a neat diffraction pattern is to employ the radiation with a wavelength analogous to the interatomic spacing in the lattice. X-rays with λ close to 1 nm are suitable to be adsorbed by engineering materials and chiefly functions to analyze crystalline structure of fine powders or small crystals [76].

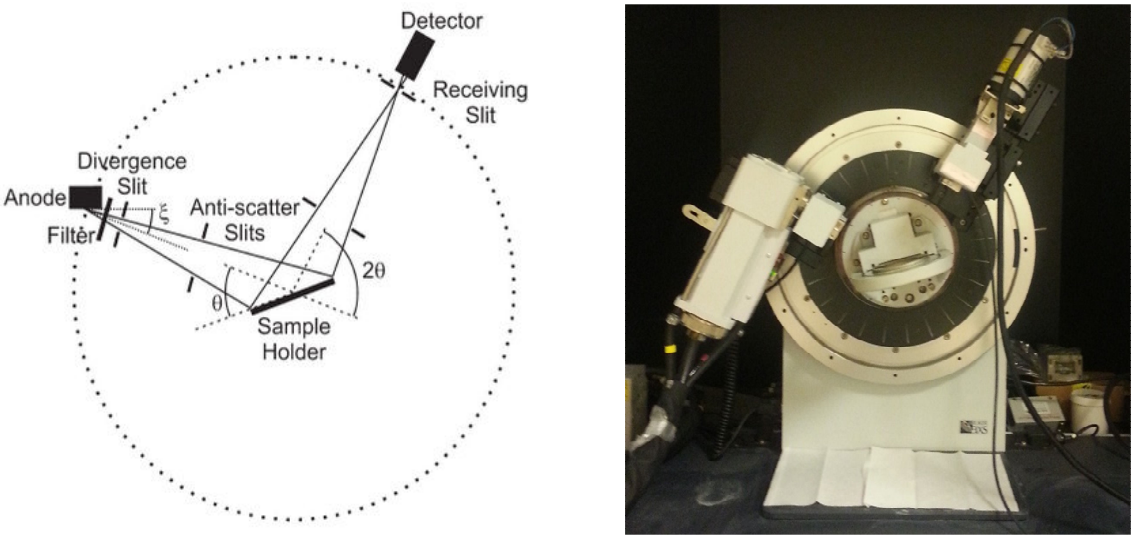

Figure 2-1. The diagram showing the working principle of an XRD [77] and (b) the XRD set up at Sabanci University.

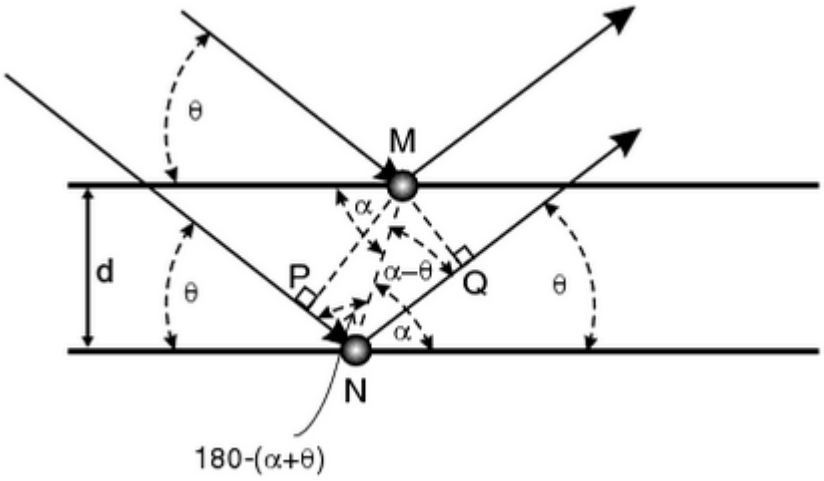

Figure 2-2. Schematic of Bragg diffraction [77]

The relationship between the angular distribution of the peak intensities in the diffraction spectrum from a regular lattice is explained by Braggs equation (Equation 2-1) [76]. The path difference created between the incident beam and the diffracted beams from two adjacent planes can be calculated with this equation where n is an integer, λ is the wavelength of X-ray radiation, d is the interlayer spacing of the crystal lattice planes and θ is the angle of the incident beam makes with lattice planes (Figure 2-2).

$$n\lambda = 2dsin\theta \qquad \text{Equation 2-1}$$

XRD measurements of Pt impregnation onto the carbon supports were performed with Bruker D-8 Advance X-Ray Diffractometer. The wavelength of irradiation of Cu Kα was 0.154 nm. The scan rate was 2.4° per min with the operating voltage of 40 kV and current of 40 mA. XRD measurements were carried out at 2θ angles from 5° to 90°.

The calculation of particle size with respect to XRD spectra is an important method invented by Debye and Scherer in 1916. The formulation is represented in Equation 2-2.

$$D = \frac{K\lambda}{\beta cos\theta} \qquad \text{Equation 2-2}$$

λ is the wavelength of the incident beam. β is the line broadening at half-maximum in radians and θ is the diffraction angle. K is the dimensionless shape factor which can be range in between 0.9 and 1 [78, 79].

2.3.1.2. *Raman Spectroscopy*

Raman spectroscopy is a vibrational spectroscopy method based on optical excitation in which the wavelength of absorbed light is different from the wavelength of emitted light [80]. This differentiation in wavelength is called as inelastic phonon scattering [81]. Vibrational transitions inside the nuclei of a molecule are inspected in Raman spectra in UV-vis region (400-800 nm). The sample is exposed to intense laser beams and scattered light which contains Rayleigh scattering and Raman scattering is generated perpendicular to the incident beam [82]. The information out of scattering and energy of vibrational transitions for different molecules inside the sample is significant in identification of sample (Figure 2-3).

Raman spectroscopy of nanoparticles was measured with Renishaw inVia Raman Spectrometer with a laser with an excitation line at 532 nm, a spectral range of 100 to 3200 cm^{-1}.

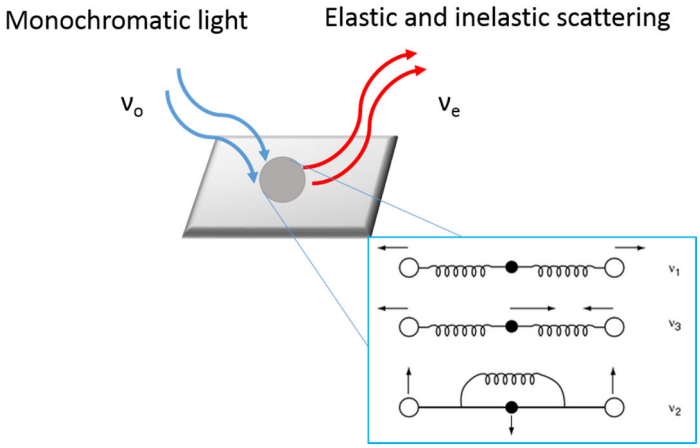

Figure 2-3. Schematic of Raman scattering and possible vibrations of a diatomic molecule [82]

2.3.1.3. *Fourier Transform Infrared Spectroscopy (FT-IR)*

Infrared (IR) spectroscopy is an effective and fast technique to extract structural information from sample in solution, liquid, solid or gaseous forms. The samples are exposed to infrared radiation which covers the part of electromagnetic spectrum between

the visible and microwave regions. In theory, the absorption of the radiation frequency less than 100 cm^{-1} by a molecule leads to energy generation of molecular rotation and this energy is converted into a form of spectra consisting of discrete lines. The absorption of radiation in the range of 100-1000 cm^{-1} results with molecular vibrations whose energies are counted and appeared as bands due to the association of vibrational energy change with the number of rotational energy changes [83]. The parameters that affects the wavelength of absorption are the relative masses of atoms, the force constants of bonds and the geometry of the atoms. The intensities of appeared bands in spectra is formulated as Equation 2-3 in terms of absorbance and transmittance.

$$A = log_{10}(1/T) \qquad \text{Equation 2-3}$$

Only the vibrations that result in a change in the dipole moment of a molecule are present in IR spectra. Functional groups with a strong dipole moment generate strong peaks in spectra.

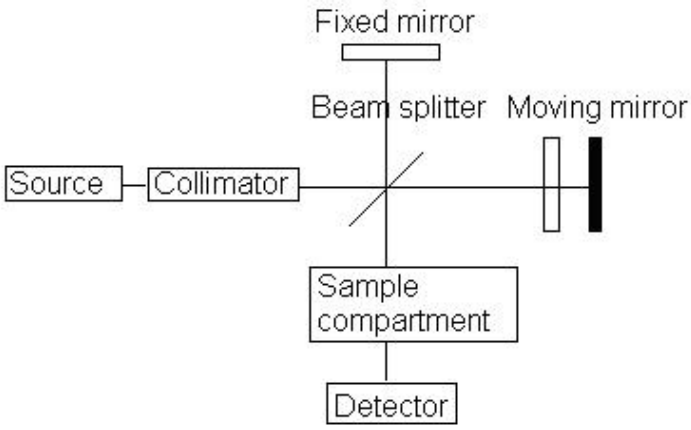

Figure 2-4. Schematic of FTIR spectrometer [84]

FTIR utilizes a radiation to be passed through the sample, containing all IR wavelengths, which is split into two beams. One beam is directed to a mirror with a fixed length and the other beam is sent to a movable mirror to vary the length. The two path lengths differ from each other and give rise to a number of constructive and destructive interferences. At the end an interferogram is obtained with a variety of intensities. Fourier Transform (FT) converts this interferogram from time domain into one spectral point on the form of frequency domain [83].

Fourier transform infrared spectroscopy (FT-IR) analyses were performed via Nicolet iS10 model spectrometer with Germanium (Ge) crystal. Samples were used in their powder form and used without further preparation.

2.3.1.4. Transmission Electron Microscopy (TEM)

TEM is a very effective technique that provides high resolution for primarily morphological studies by enlarging the imaging range from 0.3 μm to 0.15 nm [85]. It gives information on diffraction patterns of layers, defects in crystal structures, microstructure and nanoscale image of carefully prepared specimen.

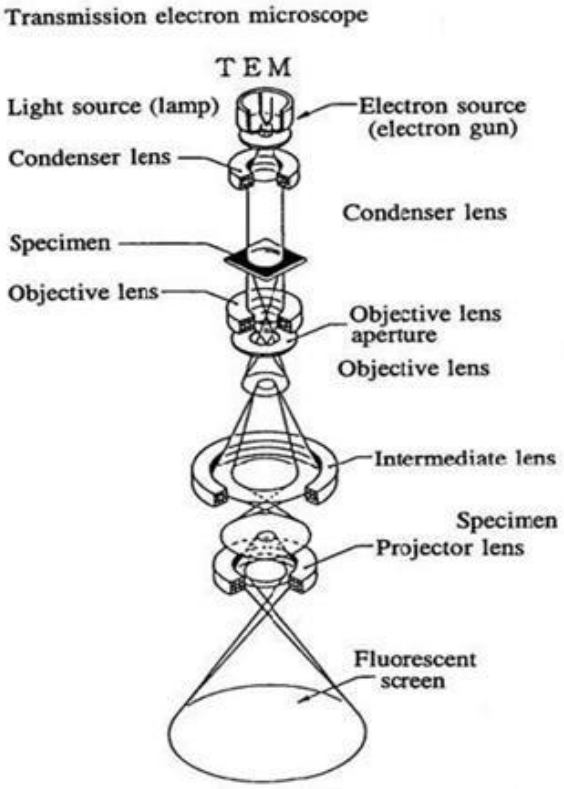

Figure 2-5. Schematic of the path of the electron beam in a TEM [86]

High energy electrons are generated by an electron gun which is made of tungsten, LaB_6. Then, generated electrons are focused onto specimen by electromagnetic condenser lens system. The resolution of the image is strongly affected by the electromagnetic lens that focuses elastically scattered electrons transmitted through specimen. Finally, image is

formed on a fluorescence screen. The measurements are conducted vacuum environment in order to avoid specimen contamination.

The morphologies of Pt nanoparticles supported with graphene and CB were characterized by using high resolution-transmission electron microscopy, JEOL 2100 JEM HRTEM.

2.3.1.5. Scanning Electron Microscopy (SEM)

Topographical images and elemental analysis of conductive specimens can be obtain effectively by using SEM. Non-conductive specimens can also be analyzed after coated with a conductive material. A beam of electrons are used in SEM to scan the surface of the specimen. Electrons are generated by applying a current to an electron gun which is mostly made of tungsten. As the current applied on electron gun, it is heated up and electrons are emitted. When the generated beam interacts with specimen, various signals which contains secondary electrons, back scattered electrons, X-rays, heat and light. Secondary electrons have relatively low energy and low penetration depth and they are detected by a radiation detector close to the surface of the specimen. Back-scattered electrons which have higher energy would be detected with another detector and provide information about the differences in atomic numbers inside the sample. At the end of signal detections and amplification, images with high magnification (10000x) and high resolution (up to 40 Å) [3].

2.3.1.6. Brunauer–Emmett–Teller (BET) Surface Area Analysis

The surface area of powders and porous structures is strongly related with measurements of physical adsorption of gas molecules on solid surfaces [87]. Brunauer–Emmett–Teller (BET) method has been widely used in determination of surface area of adsorbents, catalysts and plenty of porous materials. The specific surface area of a sample is formulated as in Equation 2-4 and used in the analysis of by physisorption isotherm data taken from multiple point measurements.

$$\frac{P/P^0}{V\left(1-P/P^0\right)} = \frac{1}{V_m C} + \frac{C-1}{V_m C}\left(P/P^0\right) \qquad \text{Equation 2-4}$$

The parameters of the Equation 2-4 are explained below:

P = partial vapor pressure of adsorbate gas in equilibrium with the surface at 77.4 K

P^0 = saturated pressure of adsorbate gas

V = volume of gas adsorbed at standard temperature and pressure (STP) [273.15 K and atmospheric pressure (1.013×10^5 Pa)]

V_m = volume of gas adsorbed at STP to produce an monolayer on the sample surface

C = dimensionless constant

The slope of t BET plot $\frac{P/P^0}{V\left(1-P/P^0\right)}$ with respect to $\left(P/P^0\right)$ enables the calculation of V_m. The specific surface area of the sample is calculated by inserting the V_m into Equation 2-5 where N is the Avogadro constant and σ is the monolayer molecular cross-sectional area specific to the adsorbate.

$$Specific\ surface\ area_{BET} = \frac{V_m}{N\sigma} \qquad \text{Equation 2-5}$$

The BET surface areas of the resultant samples were measured by Quantachrome NOVA 2200e series surface analyzer. The determination was based on the measurements of the adsorption and desorption isotherms of nitrogen at 77 K. The total surface areas were evaluated with the BET method in the P/P^0 range of 0.05–0.35. Also for all total pore volume calculations, highest P/P^0 value was selected and pore volume calculated. All samples were degassed before analysis for 24 h at 150 °C.

2.3.1.7. X-ray Photoelectron Spectroscopy (XPS)

X-ray photoelectron spectroscopy provides great information about surface structure and surface chemistry of materials. The indication of surface properties are determined by measuring the energy difference between the incident photons in a monochromatic X-rays and ejected secondary electrons after they are adsorbed by the atoms on the surface [81]. Equation 2-6 demonstrates the formulation for binding energy of photoelectron.

$$E_b = h\nu - (E_s + \phi)$$ Equation 2-6

E_s is the kinetic energy of ejected secondary electrons. The energy of incident photon is represented as hν. E_b is the binding energy of electrons that is necessary to raise the electron to the Fermi level and ϕ is the work function that is necessary to raise the electron from the Fermi level to vacuum level.

The XPS analysis were completed by Thermo Scientific X-ray Photoelectron Spectrometer with monochromatic Al Kα (hν=1486.6 eV) X-ray source. The binding energy of a photoelectron is tightly correlated with the chemical state and the same atomic species will lead to multiple peaks in the resultant spectrum due to a different coordination and binding states of this atomic species.

2.3.2. Electrochemical Characterization

2.3.2.1. Cyclic Voltammetry (CV)

Cyclic voltammetry is an electroanalytic technique which provides both thermodynamic and kinetic information about many chemical reactions. CV technique is widely used in the area of fuel cell research, chiefly in characterization of catalytic activities of materials used in fuel cell and ECSA analysis of GDLs [88].

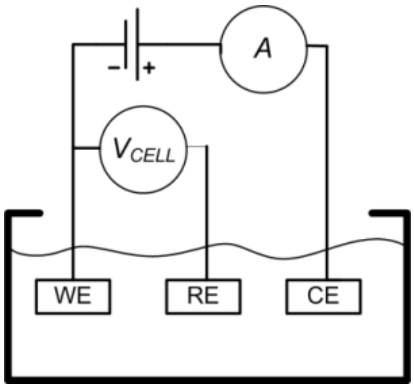

Figure 2-6. Three electrode cell system used in CV [89]

An electrochemical cell system (Figure 2-6) that contains a counter or auxiliary electrode, a reference and a working electrode, immersed into an electrolyte solution is set up to

measure cyclic voltammograms [90]. Reference electrodes (RE) are generally chosen to be Ag/AgCl or saturated calomel electrode. Counter electrodes (CE) are made of non-reactive materials and has high surface area. A platinum gauze, a graphite rod or a titanium wire can be used as counter electrodes in a three-electrode cell system. Working electrodes (WE) preferably possess a well-defined area and made of some of the following materials: Pt, Au, graphite or glassy carbon. Consequent to setting up the three electrode cell system, it is connected to a potentiostat/galvanostat. The two potential limits are selected and the cell potential is varied back and forth in between this two boundaries. A potentiostat works to control the potential difference between RE and WE with minimal interference from ohmic (IR) drop. In addition, the current that flows through the RE is aimed to be minimized in order to avoid polarization of RE and the stable applied potential distribution can be obtained between WE and RE.

ECSA is a term used to define the numbers of electrochemically active sites per gram of catalyst [91]. The total charge exchanged in H+ adsorption/desorption reactions (Equation 2-7) are determined from the integration of H^+ adsorption/desorption peaks in cyclic voltammograms after subtracting the amount of change from electric double layer region.

$$Pt - H_{ads} \leftrightarrow Pt + H^+ + e^- \qquad \text{Equation 2-7}$$

$$ECSA\ [\ cm^2 \frac{Pt}{g} of\ Pt] = \frac{Charge\ [Q_H, \mu\frac{C}{cm^2}]}{210\left[\mu\frac{C}{cm^2}\right] X\ electrode\ loading\ [g\ of \frac{Pt}{cm^2}]} \qquad \text{Equation 2-8}$$

The formulation in Equation 2-8 is utilized to calculate ECSA of different electrocatalysts by inserting the extracted charge value (Q_H) from cyclic voltammograms, electrode loading is calculated prior to CV measurements and the constant value of 210 $\mu\frac{C}{cm^2}$ represents the required amount of charge to oxidize one layer of hydrogen that is adsorbed/desorbed on Pt.

In electrochemical tests, a Ag/ AgCl electrode was used as RE, a platinum wire was chosen as CE and WE was a glassy carbon electrode (d: 3 mm) on which dispersions of synthesized electrocatalysts were placed. Cyclic voltammograms were measured by sweeping a potential region from -0.2 to 1.2 V vs. RE with a sweep rate of 50 $mV.s^{-1}$. All electrochemical tests were conducted in a N_2 purged 0.1 M $HClO_4$ solution. The amounts of the Pt catalyst in these two electrodes were maintained at 28 $\mu g.cm^{-2}$.

2.3.3. In-situ Fuel Cell Characterization

2.3.3.1. Electrode Preparation

Toray carbon paper (THP-H-030,110 μm) purchased from Fuel Cell Earth LLC in was used as gas GDL. The electrodes were prepared by ultrasonic blending 0.1 g of carbon catalyst, 0.353 g of Nafion® solution (5 wt% alcohol based from Aldrich) and 2 mL of isopropyl alcohol for 1 hour. The catalyst solution was sprayed on the surface of a single-sided uncatalyzed GDL by using a Paasche® air brush. After the catalyst was sprayed, the electrode was dried at 70°C for 30 min. The process was repeated until a total Pt loading of 0.25 $mg.cm^{-2}$ was achieved.

2.3.3.2. Membrane Electrode Assembly (MEA) Fabrication

Membrane electrode assembly (MEA) was developed by electrodes and Nafion®-NR211 membrane using hot press technique. Nafion®-NR211 membrane was preconditioned by waiting 1 hour in 3% (v:v) H_2O_2, de-ionized water, 0.5 M H_2SO_4 and then de-ionized water at 80°C respectively. MEAs with active area of 25 cm^2 were fabricated by hot pressing the cathode and anode electrodes to a pre-conditioned membrane at 120°C at 533.8 kPa for 3 minutes.

2.3.3.3. Single Cell Testing

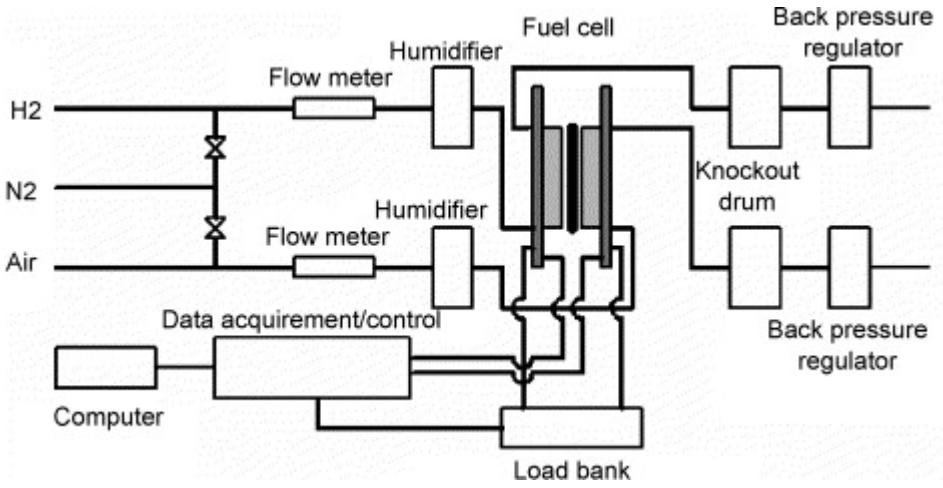

Figure 2-7. Schematic of a fuel cell test station [92]

One of the most direct and powerful method to assess the quality of a catalyst layers is single cell testing conducted inside a fuel cell test station (Figure 2-7). A fuel cell test station contains sub-systems that control several parameters such as temperature, flow rate of the reactant gases, and measures current and voltage values of the fuel cell [92]. Fuel cell station measures cell voltage adjusting current density and vice versa. Afterwards, voltage values are plotted against current density and polarization curves which are very fundamental to evaluate cell performance. The polarization curves are subsequently used to calculate power density (cell voltage times current density) [3].

The fabricated MEA was located in the test cell and a 3 Nm torque was applied on each bolt to tighten the bolts. The cell temperature was adjusted 65°C at 100% relative humidity. After the preset temperatures were reached, the cell was supplied with hydrogen and oxygen at stoichiometric ratios 1.5 and 2 for hydrogen and oxygen respectively. The cell operation voltage was set to be 0.5 V until it reached steady state. After steady state was obtained, the current-voltage data was collected with varying load starting with the open circuit value.

3. RESULTS AND DISCUSSION

3.1. Graphene Oxide Synthesis

3.1.1. XRD Results

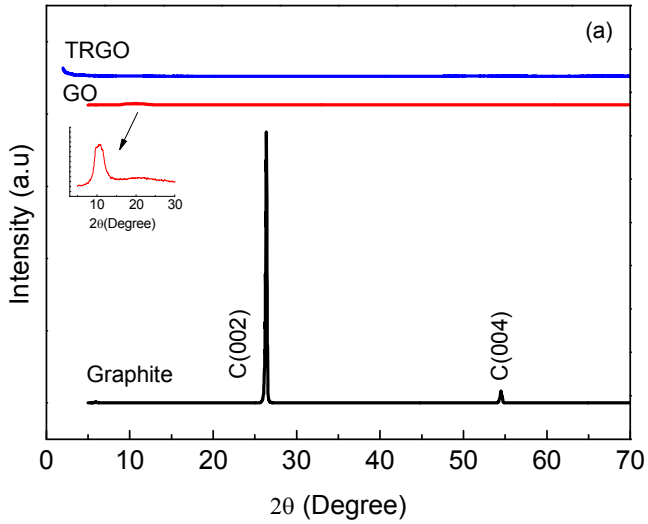

Figure 3-1. XRD spectra, graphite, GO and TRGO

The differences between XRD spectra of graphite, GO and TRGO can be found in Figure 3-1. Graphite was the precursor for the oxidation reaction. Two sharp peaks, at 2θ=26.5° and at 55°, in graphite XRD spectrum are attributed to C (002) ($d_{spacing}$=0.339 nm) and C (004) planes respectively. The latter one relates with the hexagonal lattice structure of graphite whereas the broadness of first peak implies the degree of graphitization and disorder in the structure [93]. After graphite was oxidized and GO was obtained, the peak at 2θ=26.5° was broadened and shifted to 2θ=12° ($d_{spacing}$=0.72 nm) [94]. The broadening of the peak demonstrates a disorder in graphitic structure and that would be associated with the generation of oxygen containing functionalities on the surface of graphite layers. The generation of functional groups were also responsible for the increase in the interlayer spacing of graphite from 0.339 nm to 0.72 nm.

3.1.2. Raman Results

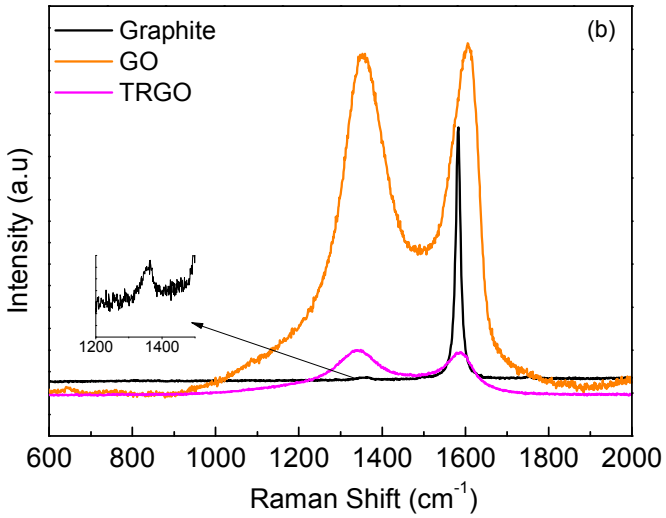

Figure 3-2. Raman spectra graphite, GO and TRGO

The indicative Raman peaks of graphitic structure are observed at ~1590 cm^{-1} (G band) which resembles an E_{2g} mode of graphite involving in-plane stretching bonds and at ~1350 cm^{-1} (D band) corresponding to A_{1g} breathing mode of graphite (Figure 3-2) [95]. The G peak was shifted up to 1610 cm^{-1} and broadened, and D peak at 1350 cm^{-1} was also broadened and intensity of it was increased as observed in Raman spectra of GO. The change in the peak intensities and width would be correlated with the reduction in the thickness of graphitic structure and deformation of ordered hexagonal lattice [41]. The intensity ratio of the D and G bands (I_D/I_G) is typically used to perceive the virtue of carbon materials [95]. The ratio of I_D/I_G increases gradually from natural graphite (0.403) to GO (1.234) indicating an increase disorder in graphitic structure with the generation of functionalities on the surface of graphite layers.

3.1.3. SEM and TEM Results

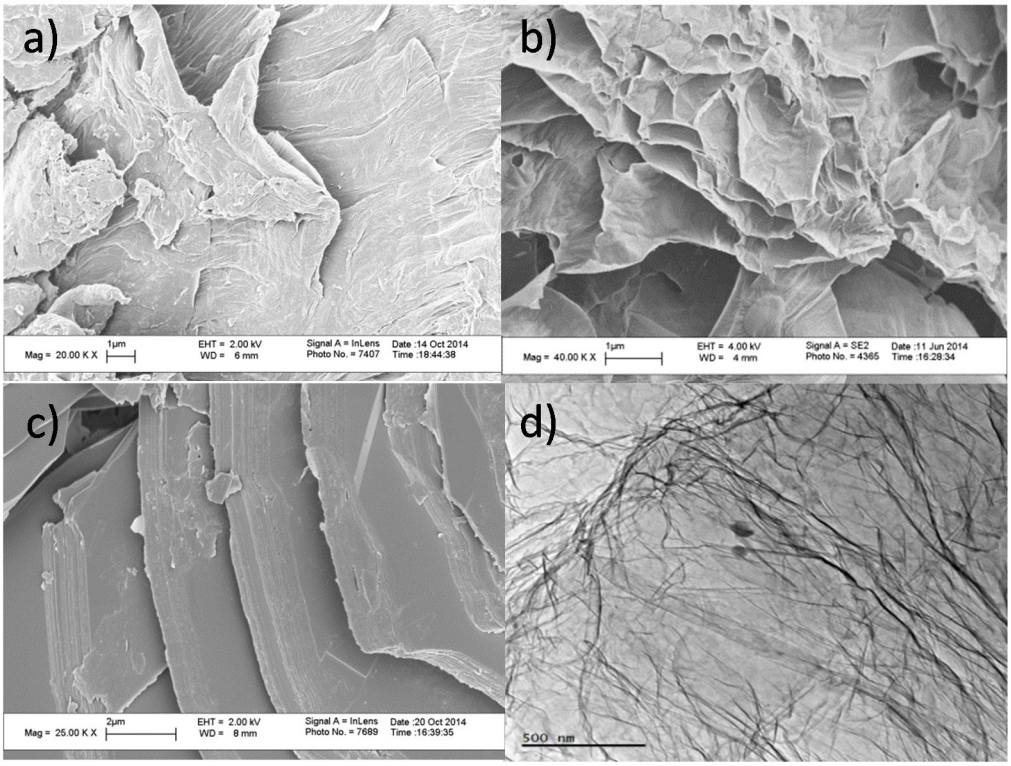

Figure 3-3.SEM image of a) Graphite flake, b) GO, c) TRGO and TEM image of d) TRGO

The morphologies of graphite flake, GO and TRGO was characterized by SEM and TEM. Figure 3-3 (a) shows SEM image of graphite flake which looks very rigid and lack of details. After oxidation of graphite, layers which are not visible in SEM image of graphite, were separated from each other due to integration of functional groups in between graphite sheets and observed in Figure 3-3 (b) SEM image of TRGO taken after thermal treatment of GO can be seen in Figure 3-3 (c) The separated layers of graphite were re-stacked to some extent, however, the presence of layers are obvious compared to graphite flakes. TEM image of TRGO in Figure 3-3 (d) revealed that thermal expansion of GO results with a crumbled transparent layers of graphite.

3.2. Comparison of Methods Used in Preparation of r-GO and GNP Supported Pt Catalyst

3.2.1. BET Results

Table 3-1. The total surface area values of samples measured by BET analysis

Sample	Total Specific Surface Area (m^2/g)	Total Pore Volume (cc/g)	Pore Size (Radius) (Å)
Graphene platelet	759.4	1.321	>551.0
Pt-GN-Ethylene glycol	680.2	1.114	>605.3
FGN-citric acid-Pt	458.2	0.873	>572.5
$NaBH_4$ red-GN/Pt	649.9	1.069	>545.9

Table 3-2. The surface area of samples by BJH analysis

Sample	Surface Area (m^2/g)	Pore Volume (cc/g)	Pore Size (Å (Radius))
Graphene platelet	762.8	1.254	>10.99
Pt-GN-Ethylene glycol	495.6	0.991	>10.09
FGN-citric acid-Pt	415.3	0.758	>15.78
$NaBH_4$ red-GN/Pt	339.1	0.877	>17.958

The BET analysis of N_2 desorption-absorption isotherms of GNP and GNP supported Pt nanoparticles are demonstrated in Table 3-1. The total specific surface area of GNP was measured as 759.4 $m^2.g^{-1}$ from multi point BET analysis, and pore volume was recorded as 1.321 $cc.g^{-1}$. The effect of Pt decoration on GNP was aimed to be investigated and for that purpose, the surface areas of GNP supported Pt nanoparticles which were prepared via different methods were compared. The closest total SSA value to total SSA of GNP between all prepared electrocatalysts was obtained from the sample that was reduced with ethylene glycol and it was noted as 680.2 $m^2.g^{-1}$. Nanoparticles prepared by NaBH4 reduction has a relatively low total SSA of 649.9 $m^2.g^{-1}$. FGN/Pt had a total SSA of 458.2

$m^2.g^{-1}$ which can be framed as a dramatic deviation from total SSA of GNP. Total pore volume of the samples demonstrated a similar behavior with total SSA by decreasing after Pt decoration and the amount of decrease between the samples was also comparable with the sequence experienced in the case of total SSA. Pore size of the samples were measured in between 50 to 60 nm according to multi point BET analysis. These values may be attributed to the presence of mesopores (d: 2-50 nm). Additionally, the Barret–Joyner–Halenda (BJH) desorption analysis revealed that pores whose diameter below 2 nm and these were attributed to the presence of micropores in the structure (Table 3-2). A descending trend in the fraction of mesopores and ascending trend in micropores were observed after Pt decoration on GNP.

The functionalization of GNP was reported to decrease the total SSA [96, 97] and the authors explained that behavior with an increase in the GNP density in the presence of other particles. The decrease in the total SSA also may be correlated with the stacking of layers of GNP after the reduction process. Stacking of layers prevents the accessibility of N_2 to each layer and adsorption-desorption values of only the outside layers and edges would be measured resulting with a lower SSA. Although Pt decoration of GNP via ethylene glycol and $NaBH_4$ methods resulted with very close SSA values, functionalized GNP was distinguished from them. Here, the functionalization with citric acid should be underlined as ineffective in terms of the protection of SSA during the Pt decoration.

3.2.2. FTIR Results

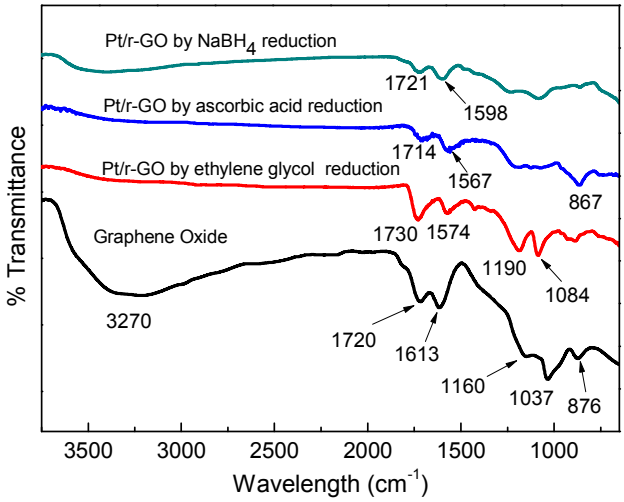

Figure 3-4. FTIR Results of Pt/r-GO prepared by various Pt impregnation methods

The chemical structures of GO and the GO supported electrocatalysts were examined with FTIR and the results were compared as seen in Figure 3-4. FTIR spectra of GO contains a broad peak around 3270 cm^{-1}. Additionally, sharp peaks at 1720, 1613, 1160, 1037 and 876 cm^{-1} are observed. The broad peak is attributed to O-H stretching of carboxylic acid groups. The peak at 1720 cm^{-1} can be correlate with aromatic stretching of carbonyl groups in the chemical structure of GO. The presence of C=C groups in GO layers give rise to the peak at 1613 cm^{-1}. The peaks at 1160 and 1037 cm-1 are most probably observed due to in-plane stretching of C-H or stretching of C-O in cyclic ether groups that can be seen in the chemical structure of GO (Figure 3-5). The last peak is present due to out-of-plane stretching of C-H [98].

The main difference between GO spectra and other GO supported electrocatalysts is the presence of broad peak representing O-H stretching of carboxyl group. Most oxygenated functional groups, mainly carboxyl groups, disappeared during reduction process [99].

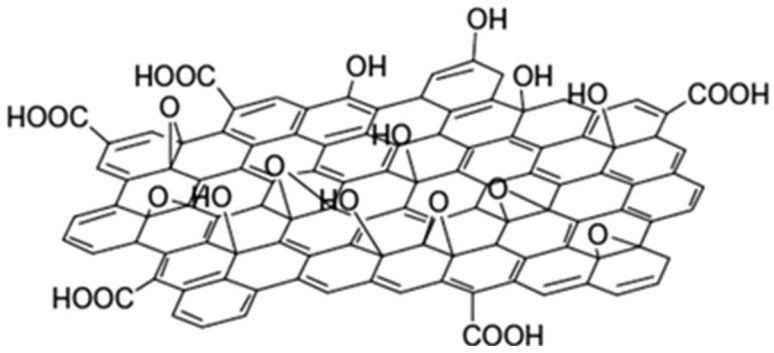

Figure 3-5. Chemical structure of graphene oxide [99]

Electrocatalysts prepared by ethylene glycol reduction prevents the all peaks in GO spectra except the one at 3270 at cm^{-1} whereas the broad peak responsible for O-H stretching. The spectra of Pt/r-GO by ascorbic acid reduction contains peaks at 1714, 1567, and 867 cm^{-1}. The peaks at 1160 and 1037 cm^{-1} in GO spectra are seemed to be broadened here and disappeared. In the case of Pt/r-GO by $NaBH_4$ reduction, most visible peaks are at 1721 and 867 cm^{-1}. The O-H peak is also slightly visible in that spectra. The comparison of reduction methods distinguishes NaBH4 method to be less effective than other two methods as the carboxyl groups are not completely disappeared. However, all three methods seem quite effective to decrease the number of functional groups on the surface of GO. The functional groups on the surface of GO is reported as a positive effect to nucleate nanoparticles [16] and after a reduction takes place functional groups are

occupied with Pt nanoparticles. The decrease in the number of functional groups would also suggest a clear prediction on effective reduction of Pt nanoparticles on GO.

3.2.3. XRD Results

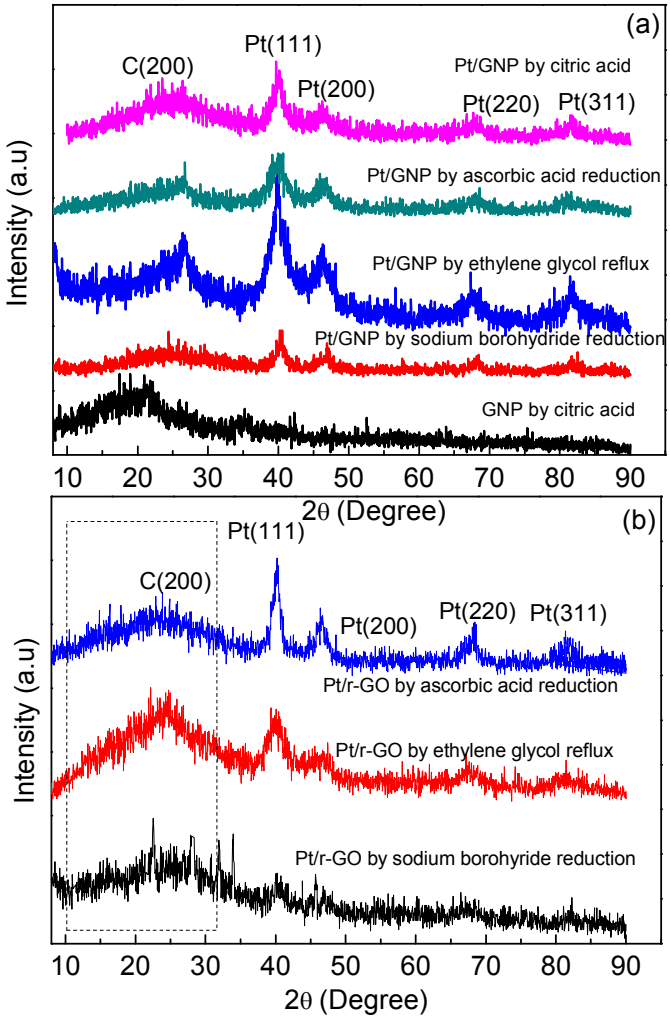

Figure 3-6. XRD spectra of various Pt impregnation methods on a) GNP, b) GO

XRD spectra of Pt/GNP and Pt/r-GO can be seen in Figure 3-6 (a) and (b) respectively. The peak at 2θ=26.23° is associated with (0 0 2) diffraction peak of graphitic structure [100]. This peak was generated via the movement of characteristics peak of GO at 2θ=12° at the end of reduction process. Amorphous structure of GO was transformed into a more crystalline form and a sp^2 carbon network was regenerated [56].

Successful Pt decoration on GNP and GO was confirmed by analysis of XRD spectra. The peaks at 2θ= 39.5, 46.2, 67.1°, and 81.2° are implicated to the (111), (200), (220),

and (311) crystalline planes which indicate face-centered-cubic structure of Pt. The differentiation of Pt peak intensities may attract attention and would be correlated with the effectiveness of reduction method. The sharpest peaks between the samples where GNP was used as the catalyst support were observed in Pt/GNP prepared via ethylene glycol. Among the electrocatalysts where GO was used as the catalyst support, the highest intensity of Pt peaks were observed for ascorbic acid reduction method. However, the comparison of peak intensities might be misleading as non-homogenous dispersion of Pt nanoparticle on top of carbon supports might result with high intensities independent of the preparation methods.

Table 3-3. Platinum particle size calculation with Debye-Scherer equation

Sample Name	**d(nm)**
Pt/GNP by citric acid functionalization	8.7
Pt/GNP by ethylene glycol reflux	6.3
Pt/GNP by $NaBH_4$ reduction	6.5
Pt/GNP by ascorbic acid reduction	4.8
Pt/r-GO by $NaBH_4$ reduction	8.5
Pt/r-GO by ascorbic acid reduction	7.4
Pt/r-GO by ethylene glycol reflux	4.7

Average Pt nanoparticle size was calculated by Debye-Scherer equation ($d=0.89\,\lambda/\,\beta\cos\theta$) in which Bragg angles, θ, obtained from Pt (111) peak were inserted [101, 102]. The calculated values are presented in Table 3-3. The smallest particles with a diameter of 4.8 nm were obtained by ascorbic acid reduction of Pt/GNP. In the case of Pt/r-GO, ethylene glycol was found to be effective to reduce particle size down to 4.7 nm.

3.2.4. Raman Results

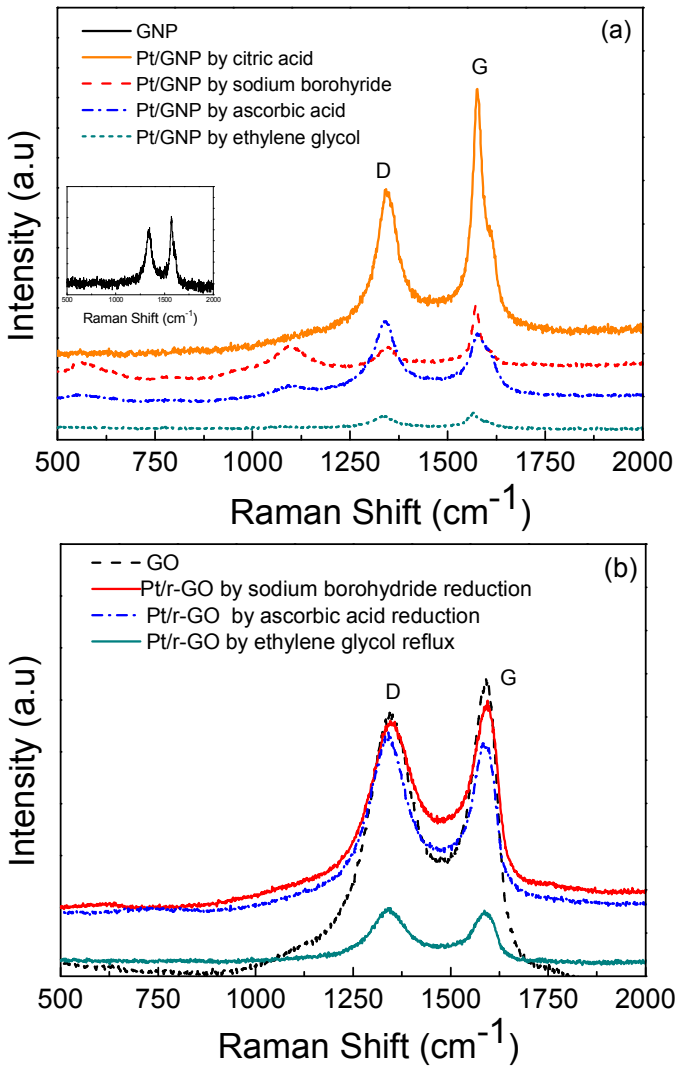

Figure 3-7. Raman Spectroscopy results of Pt impregnation on a) GNPs, b) GO

Raman spectroscopy results of Pt deposition on GNP supports and GO supports are demonstrated in Figure 3-7 (a) and (b) respectively. The characteristic peaks of graphitic structures are the G peak around 1340 cm^{-1} which is generated due to sp^2 hybridized carbon atoms and D peak around 1590 cm^{-1} which is generated due to sp^3 hybridized carbon atoms of disordered graphene [60]. The intensities of G and D peaks and the comparison of them provide a significant information about structural organization of atoms. Ferrari *et al.* documented that in amorphous carbon structures, broadening of D peak might be associated with distortion of aromatic ring in other words a decrease in the number of sp^2 hybridized domains [95]. The ratio of D peak intensity to G peak intensity is mostly used as a parameter to define the disorder amount in carbon materials.

Table 3-4. Calculated I_D/I_G ratios for various methods

Sample	I_D/I_G ratio
Pt/GNP by citric acid functionalization	0.88
Pt/GNP by $NaBH_4$ reduction	0.87
Pt/r-GO by $NaBH_4$ reduction	0.94
Pt/GNP by ascorbic acid reduction	**0.99**
Pt/r-GO by ascorbic acid reduction	1.02
Pt /GNP by ethylene glycol reflux	0.92
Pt/r-GO by ethylene glycol reflux	**1.05**

I_D/I_G ratio were calculated with respect to Raman spectra and showed in Table 3-4. The samples were compared according to reduction methods while keeping the catalyst support the same. As long as the catalyst supports are the same, Pt decoration of these supports would create defects and the I_D/I_G ratio would differentiate in each sample related with the introduction of Pt nanoparticles into the structure of support material. The D peak intensity increases with the interaction of graphene lattice with metal nanoparticles resulting with defects in the structure [103, 104] . The unloaded catalyst supports GO and GNP owns I_D/I_G ratio of 0.89 and 0.80 (± 0.01) respectively. The Pt decoration in both of the groups resulted with an increase in I_D/I_G ratio supporting the defect generation. In either case, the reduction methods were concluded to be more effective if the Pt decoration leads to a higher defect in graphene structure. In between the samples where GO was used as catalyst support, the highest I_D/I_G ratio was observed in Pt/r-GO by ethylene glycol reflux and Pt/GNP by ascorbic acid reduction had highest I_D/I_G ratio in between the samples where GNP was used as catalyst support. The type of catalyst support is a parameter in choosing the most effective method in Pt reduction.

3.2.5. TEM Results

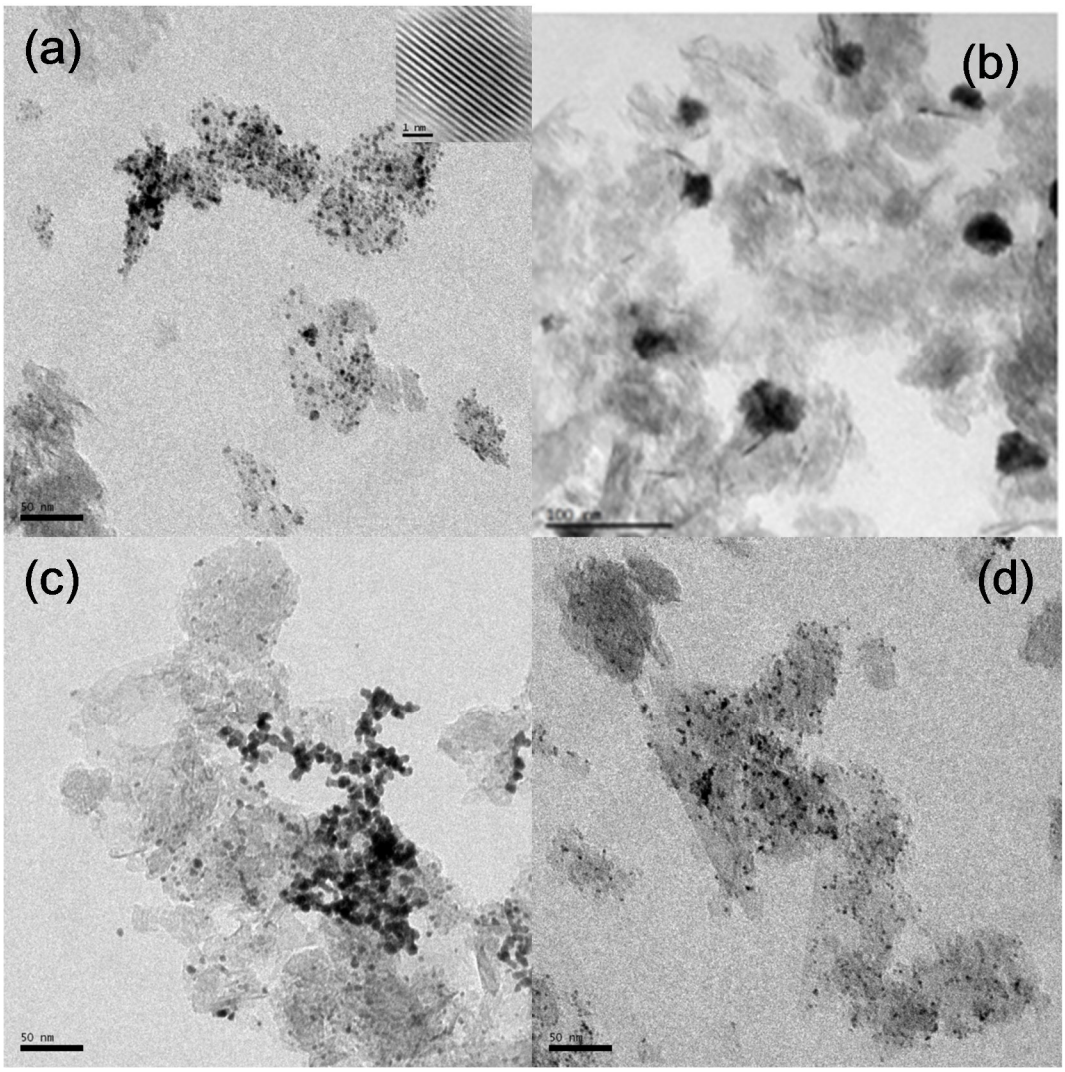

Figure 3-8. TEM images of Pt/GNP nanoparticles by a) ethylene glycol reflux and b) sodium borohydride reduction c) citric acid functionalization d) ascorbic acid reduction

The homogeneity of Pt dispersion on carbon supports and particle size of Pt were aimed to be figured out with TEM analysis. TEM images of Pt/GNP nanoparticle which were prepare via different reduction methods can be seen in Figure 3-8. The dispersion of Pt on GNP was achieved successfully by ethylene glycol reflux and ascorbic acid reduction in Figure 3-8 (a) and (d) whereas TEM images of $NaBH_4$ reduced Pt/GNP and citric acid functionalized Pt/GNP demonstrated agglomeration of Pt nanoparticles. Agglomeration of nanoparticles results with a larger diameter. Calculated particle size values from Debye-Scherer equation for $NaBH_4$ reduced Pt/GNP and citric acid functionalized Pt/GNP were 6.5 and 8.7 nm which seems quite compatible with TEM results.

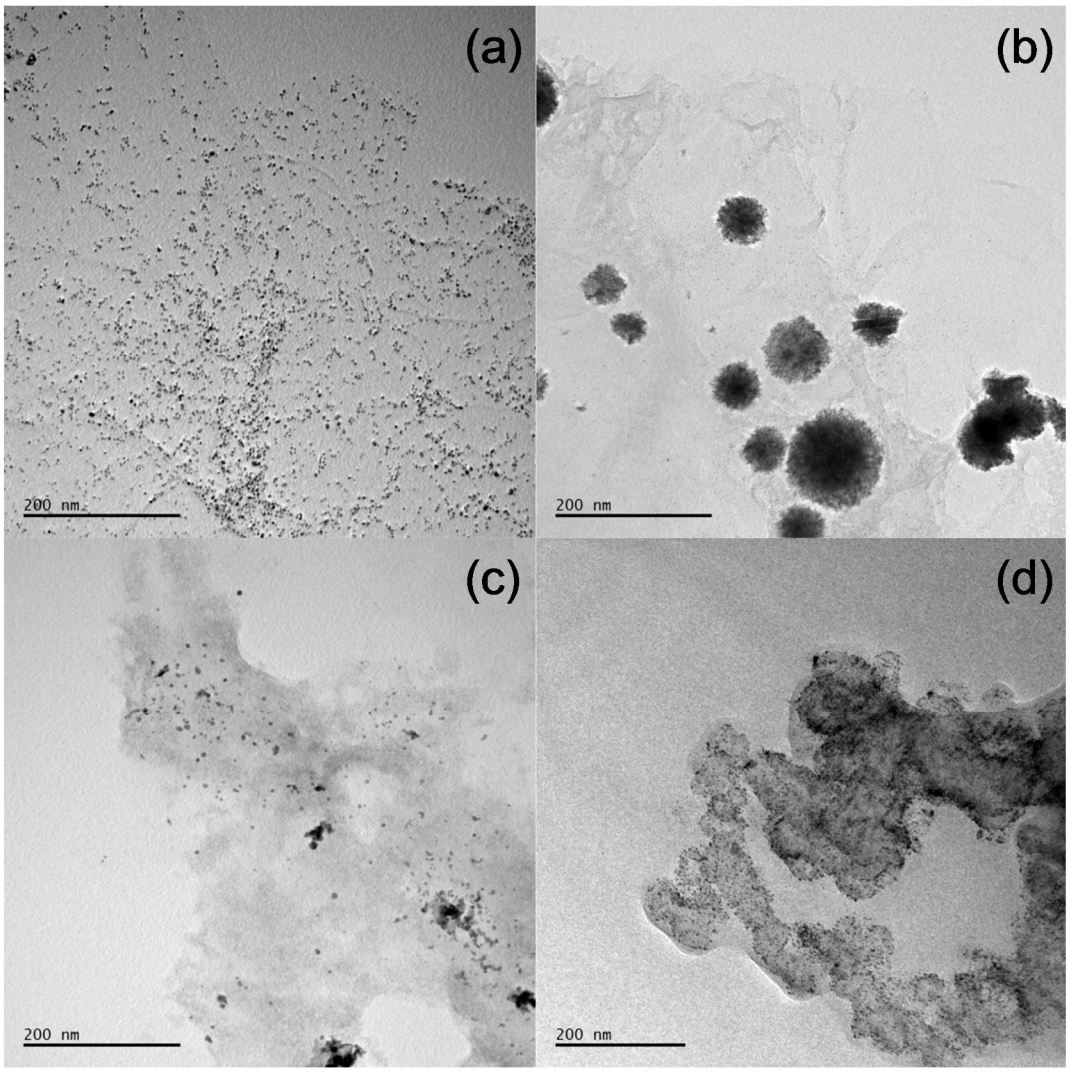

Figure 3-9. TEM images of Pt/r-GO nanoparticles by a) ethylene glycol reflux b) ascorbic acid reduction c) sodium borohydride reduction and d) Pt/ Vulcan by ethylene glycol reflux

Reduction methods has an influence on the dispersion of Pt nanoparticles on GNP and GO supports. Figure 3-9 shows TEM images of Pt/r-GO prepared by various methods. Ethylene glycol reflux seems to be very promising as having an extremely homogenous distribution of Pt nanoparticles on graphene sheets. Ascorbic acid and NaBH4 reduction methods were unable to disperse Pt nanoparticles and ended up with Pt agglomerations having large diameters as large as 40 nm. Figure 3-9 (a) is TEM image of Pt nanoparticles supported with commercial Vulcan prepared by ethylene glycol reflux. Comparison of Figure 3-9 (a) and (d) provides the evidence GO might be a better candidate than Vulcan as having a larger area for Pt nanoparticles to be distributed homogenously.

3.3. Comparison of Pt Precursors

In section 3.2, comparison of Pt reduction methods on GNP and GO provides a very large insight about efficient preparation of electrocatalysts and some of the methods have distinguished from other methods. According to XRD results ascorbic acid and ethylene glycol reflux methods were found very effective in Pt impregnation. Additionally, TEM results showed that homogenous distribution of Pt nanoparticles with smaller sizes were obtained by ethylene glycol reflux for both GNP and GO containing samples. BET, FTIR and Raman results were also supported that ethylene glycol reflux was effective in Pt impregnation on GNP and GO supports. The research was directed to the comparison of Pt precursors on GO, TRGO and Vulcan supports by employing the reduction method which was found effective in reduction.

3.3.1. XRD Results

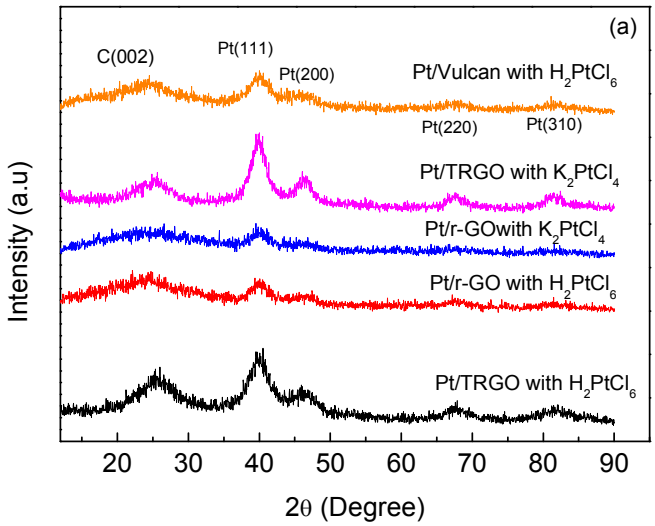

Figure 3-10. XRD spectra of samples prepared by different Pt precursors

In Figure 3-10, XRD spectra of Pt/r-GO, Pt/TRGO and Pt/Vulcan samples which were prepared by using two different Pt precursors which are H_2PtCl_6 and K_2PtCl_4 is demonstrated. Among the Pt peaks, the one around 2θ=39.5° that represents (111) crystal plane was pointed out to be highly conspicuous and present in all of the samples indicating that Pt was successfully reduced to its metallic form. Other peaks at 2θ= 46.7°, 68°, and 82° which are attributed to the (111), (200), (220), and (311) fcc planes were additionally

distinctive for Pt/TRGO with K_2PtCl_4, Pt/TRGO with H_2PtCl_6 and Pt/Vulcan with H_2PtCl_6 whereas Pt/r-GO samples slightly showed these peaks in their XRD spectra. The specific C (002) peak is present in all the samples, however, the broadness of the peak differentiates. In the samples where GO was used as catalyst support, the C (002) peak was generated after C (001) peak elimination due to reduction, however, the partial reduction of oxygen containing functional groups might result with a wider peak covering a range of different oxidation states. On the other hand, TRGO has a sharper C (002) peak which points out highly ordered graphitic structure with less amount of sp^3 domains.

3.3.2. Raman Results

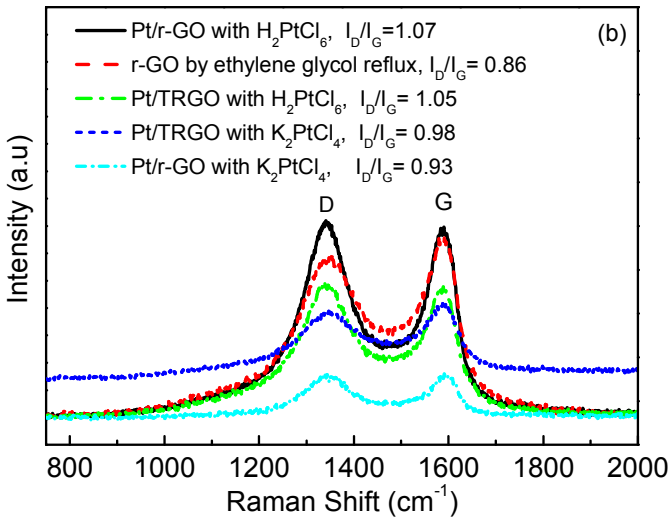

Figure 3-11. Raman Spectra samples prepared by different Pt precursors

The Raman spectra of Pt/r-GO and Pt/TRGO prepared utilizing K_2PtCl_4 and H_2PtCl_6 is shown in Figure 3-11. The characteristic peak of graphitic structure, G, and the peak representing the defect amount in the structure, D, is observed at 1590 cm^{-1} and 1340 cm^{-1} respectively. The calculated I_D/I_G were compared in Table 3-5 and highest ratio was discovered to be 1.07 for Pt/r-GO with H_2PtCl_6 suggesting that highest Pt decoration was achieved while disturbing the graphene lattice.

Table 3-5. Calculated I_D/I_G ratios for different Pt precursors

Sample	I_D/I_G ratio
r-GO by ethylene glycol reflux	0.86
Pt/r-GO with H_2PtCl_6	**1.07**
Pt/TRGO with H_2PtCl_6	1.05
Pt/r-GO with K_2PtCl_4	0.98
Pt/TRGO with K_2PtCl_4	0.93

3.3.3. TEM Results

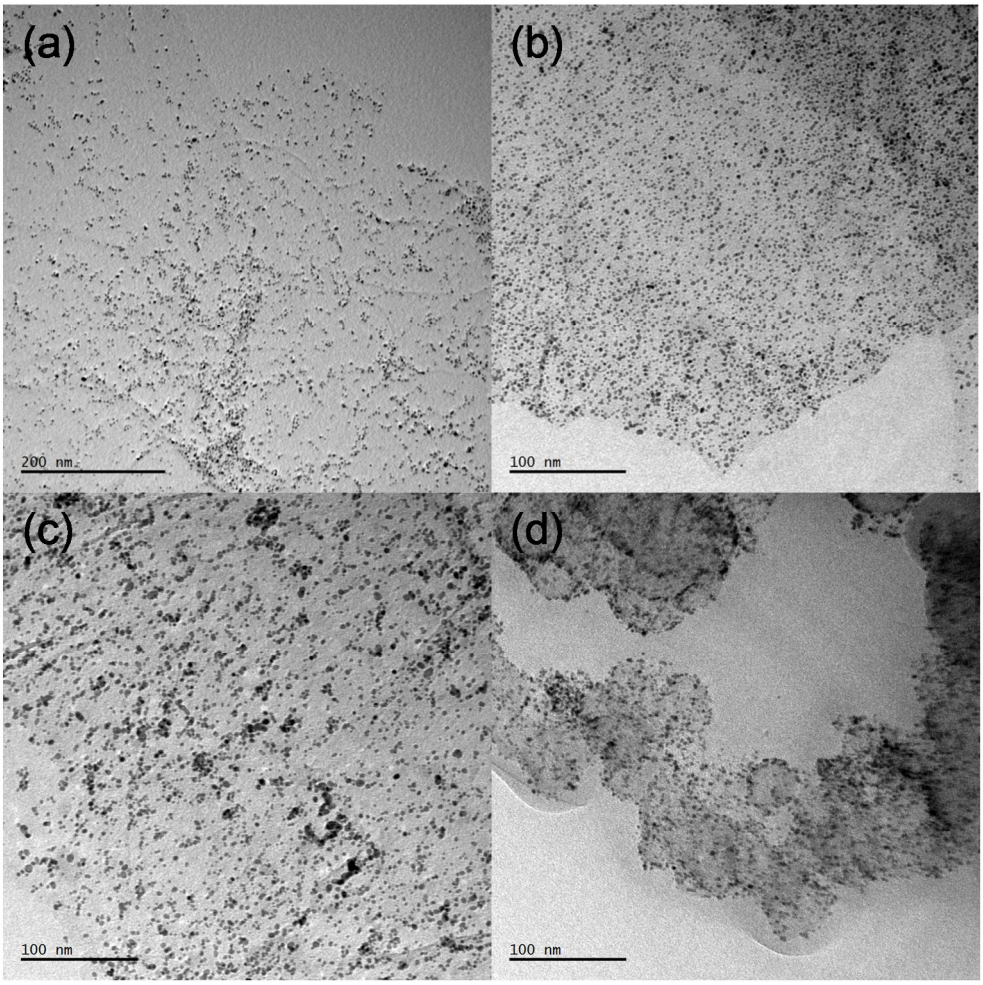

Figure 3-12. TEM micrographs of ethylene glycol reduction a) Pt/r-GO with H_2PtCl_6 precursor b) Pt/TRGO with H_2PtCl_6 precursor c) Pt/TRGO with K_2PtCl_4 d) Pt Vulcan with H_2PtCl_6

The distribution of Pt nanoparticles were analyzed with TEM. Figure 3-12 (a) maintains a perfectly distributed Pt nanoparticles on top of thin layer of graphene sheets and average particle size of Pt/r-GO with H_2PtCl_6 proved to be smaller compared to other samples free from agglomerated Pt clusters with large diameters. The comparison of Figure 3-12 (b) and (c) implies that utilizing H_2PtCl_6 in Pt deposition on top of TRGO provides a better Pt distribution and lower Pt particle size. Figure 3-12 (d) shows Pt decoration pattern on Vulcan with H_2PtCl_6 and Pt agglomeration is one of the outcomes from that TEM image. The comparison of this image with other ones would bring the conclusion that Pt decoration of graphene supports results with a better distribution than CB supports.

The differences in the degree of Pt reduction by utilization of H_2PtCl_6 versus K_2PtCl_4 might be related with the reduction mechanism of Pt (IV) and Pt (II). The reduction of H_2PtCl_6 is a two-step process in which Pt (IV) reduces to Pt (II) and then reaches to its metallic form. This reduction mechanism is demonstrated in Equation 3-1 and 3-2.

$$PtCl_6^{2-} + 2e^- \rightarrow PtCl_4^{2-} + 2Cl^- \qquad \text{Equation 3-1}$$

$$PtCl_4^{2-} + 2e^- \rightarrow Pt^0 + 4Cl^- \qquad \text{Equation 3-2}$$

The equilibrium of H_2PtCl_6 reduction is reached after a relatively long time [105]. Pt in metallic form starts to deposit on graphene supports as the reduction starts. When the reduction methods and Pt precursor amount is the same, the initial deposition of Pt would be higher in the case of K_2PtCl_4, and Pt is susceptible to be agglomerated due to limited reduction time. In the case of H_2PtCl_6, the initial Pt deposited on the surface of graphene would be low while Pt (II) ions are still present in the medium and they might be dispersed all over the graphene surface likely to find and attach to the unoccupied parts of the surface. This reasoning is supported by the TEM images of Pt/GNP and Pt/r-GO with H_2PtCl_6 exhibiting highly distributed Pt nanoparticles with lower particle size.

3.4. XPS Results

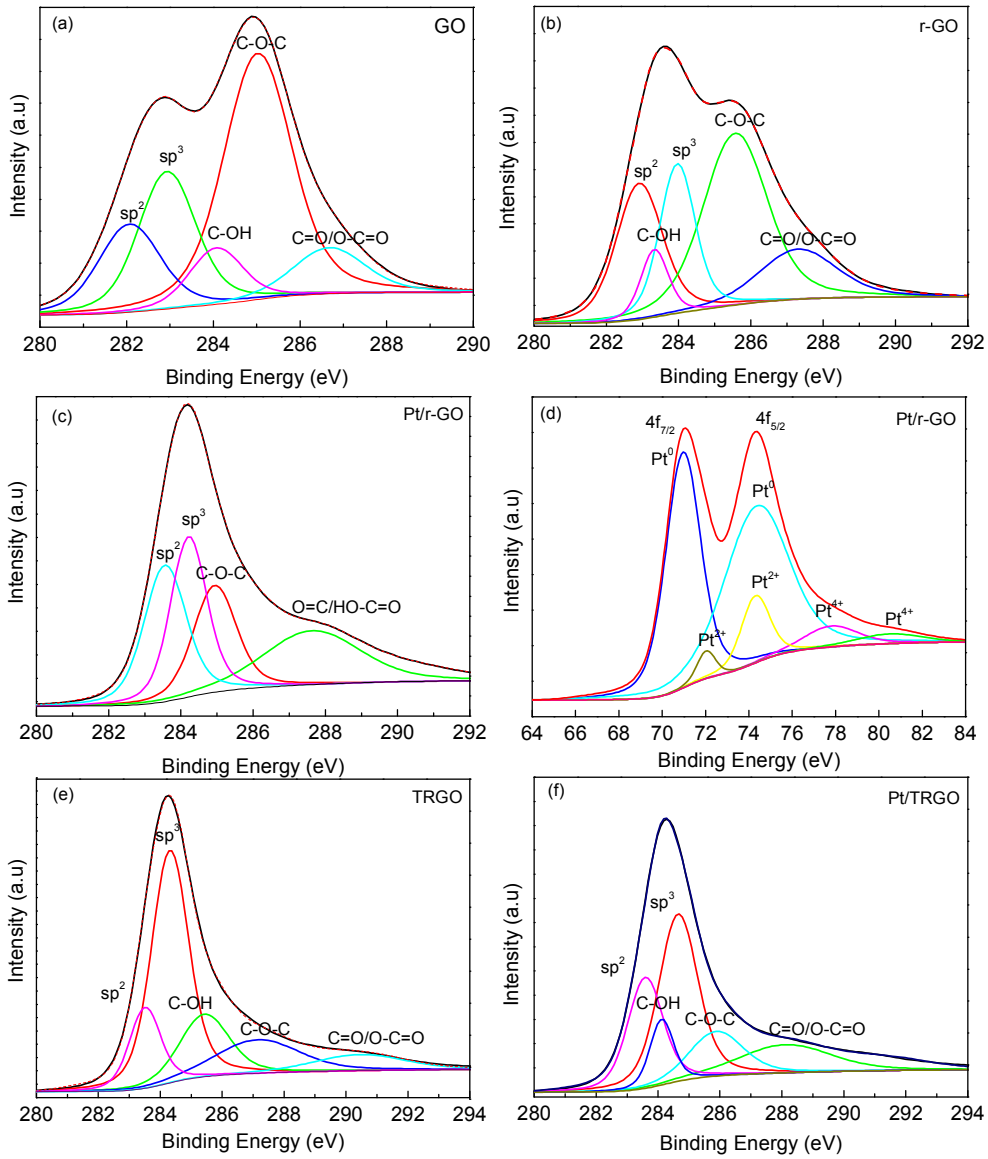

Figure 3-13. High resolution de-convoluted XPS spectra a) C1s for GO b) C1s for r-GO c) C1s for Pt/r-GO d) Pt 4f for Pt/r-GO e) C1s for TRGO f) C1s for Pt/TRGO

Chemical structure of GO, TRGO, Pt/GO and Pt/TRGO was analyzed with XPS and exhibited in Figure 3-13. The C1s XPS peak of GO is de-convoluted into five types of peaks such as C=C (sp^2), C-C (sp^3), C-OH, O-C-O and C=O/O-C=O corresponding to the binding energy of around 282, 282.93, 284.07, 285.02, and 286.66 eV, respectively, which coincides with oxidized functional groups including hydroxyl (C-OH), epoxy-ether (C-O-C) and carbonyl-ketone, carboxyl (C=O/O-C=O) that are present in GO [54]. Figure 3-13 (b) demonstrates partial reduction of oxygenated surface functional groups

on GO and restoration of sp^2 domains due to ethylene glycol reduction. Pt/r-GO samples contains a dominant peak of C=C/C-C whereas peak intensity of functional groups in the range of 283-290 eV dramatically decreases due to the interaction Pt nanoparticles with functional groups during Pt impregnation on GO [54, 100]. De-convoluted Pt 4f spectra of Pt/r-GO is displayed in Figure 3-13 (d) providing peaks representing three oxidation states of Pt. Peaks at 70.9 eV (Pt 4f7/2) and 74.36 eV (Pt 4f5/2) are the characteristic of the metallic Pt^0. Peaks centered at 71.8 eV (Pt 4f7/2) and 76.8 eV (Pt 4f5/2) are the indication of the Pt^{II}, and the broad peaks at 77.7 eV is assigned to the Pt^{IV} species.

Comparison of Figure 3-13 (a) and (e) illustrates successful removal of oxygen containing surface groups which functions as Pt anchoring sides for impregnation process, and additionally points out an increase in the amount of sp^3 domain size due to the generated defects during removal of surface functional groups [106, 107]. Absence of oxygen containing surface groups constitutes a drawback for Pt attachment on the surface. Figure 3-13 (f) also shows the partial restoration of sp^2 domains which were achieved simultaneously with Pt impregnation on TRGO.

3.5. Electrochemical Test Results

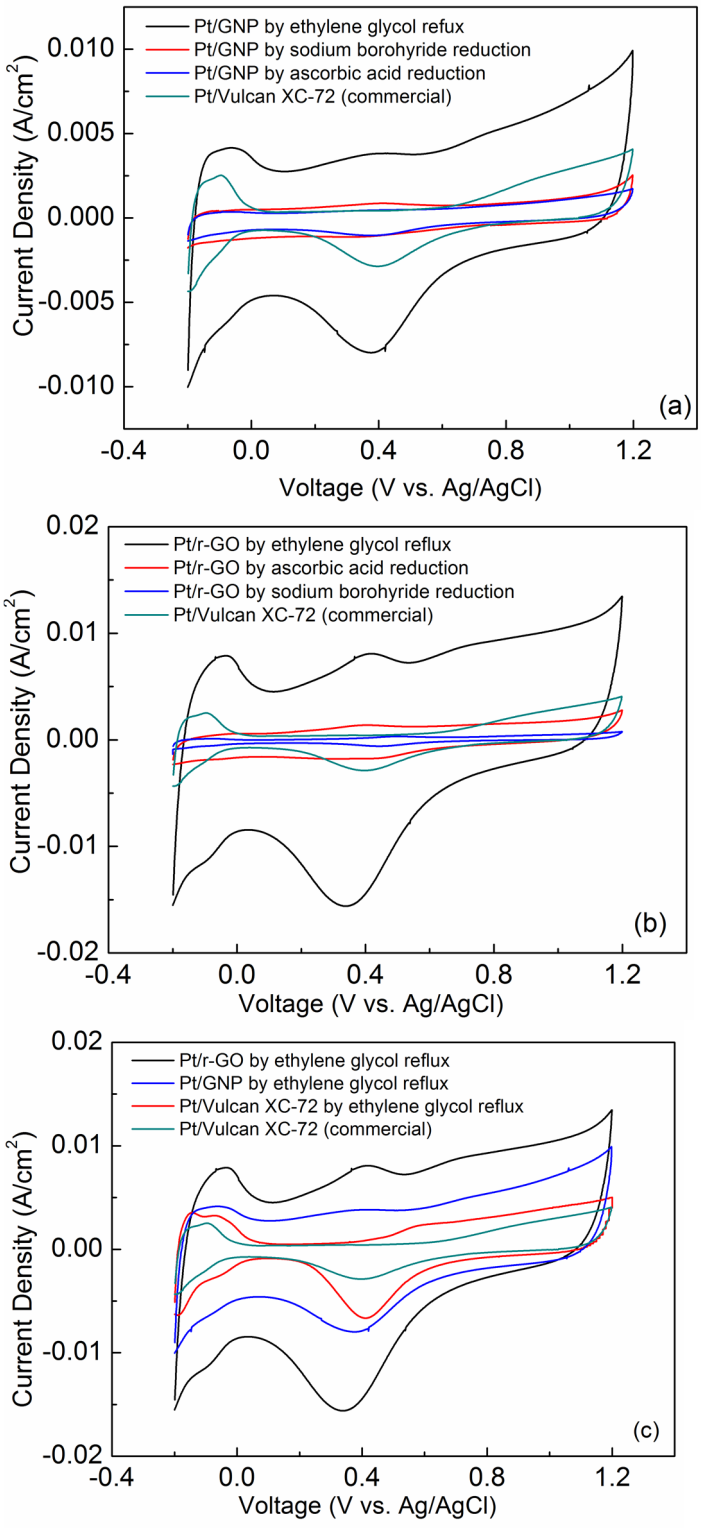

Figure 3-14. Cyclic voltammograms of a) Pt/GNP b) Pt/r-GO c) Comparison of Pt/r-GO by ethylene glycol refluxed nanoparticles with commercial Pt/Vulcan and Pt/Vulcan by ethylene glycol reflux.

Cyclic voltammograms of Pt/GNP, Pt/r-GO, Pt/Vulcan prepared by ethylene glycol reflux and commercial Pt/Vulcan is demonstrated in Figure 3-14. The intensities of hydrogen adsorption and desorption peaks of polycrystalline Pt that are present in voltammograms are firmly informative about electrocatalytic activities of catalyst nanoparticles. The peaks at CV of Pt/GNP prepared by ethylene glycol reflux have attracted attention due to having highest intensity compared to Pt/GNP prepared by other methods. Ethylene glycol method is also produced the Pt/r-GO with highest electroactive material compared to the other Pt reduction methods on GO. To fulfill a further comparison among the most promising methods according to their electroactivity, Pt/Vulcan prepared by ethylene glycol reflux, and Pt/GNP and Pt/r-GO are compared with both commercial Pt/Vulcan and Pt/Vulcan prepared by ethylene glycol reflux in Figure 3-14 (c). The Pt/r-GO by ethylene glycol reflux has an immense superiority over other samples. Additionally, the positive effect of ethylene glycol reflux is pronounced throughout the comparison of commercial Pt/Vulcan with the synthesized Pt/Vulcan via ethylene glycol reflux.

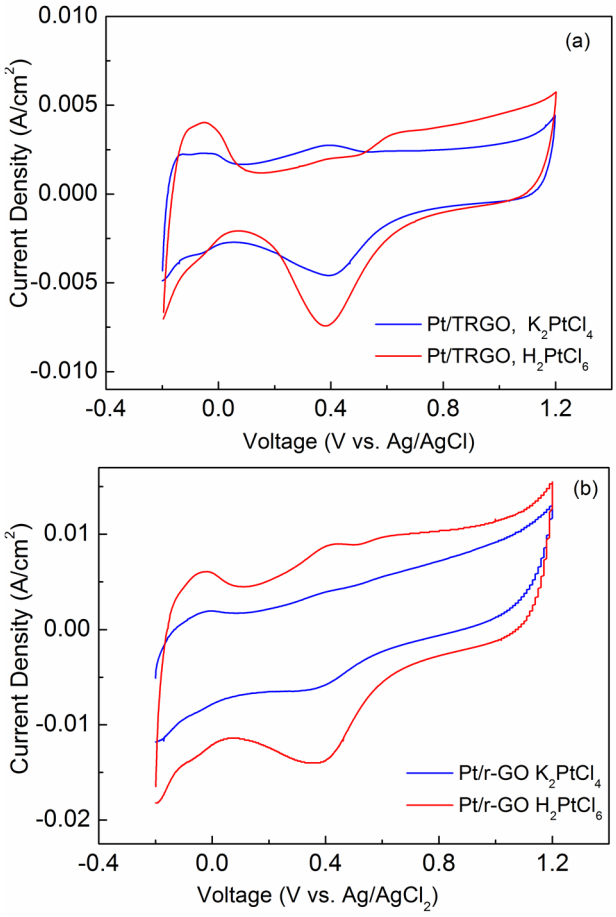

Figure 3-15. Cyclic voltammograms of a) Pt/r-GO b) Pt/TRGO, with different Pt precursors

The impact of using a different Pt precursor (K_2PtCl_4) for GO and TRGO supports was also aimed to be investigated. Cyclic voltammograms of Pt/TRGO and Pt/r-GO samples using both K_2PtCl_4 and H_2PtCl_6 prepared by ethylene glycol reflux were measured and shown in Figure 3-15. Both Pt/r-GO and Pt/TRGO prepared in the presence of H_2PtCl_6 showed higher hydrogen adsorption/desorption peaks.

Area under the peaks of CV is utilized to calculate ECSA of Pt/GNP, Pt/r-GO and Pt/Vulcan and calculated values are displayed in Table 3-6. The highest ECSA, 148 $m^2.g^{-1}$, is calculated for Pt/r-GO by ethylene glycol reflux which is 55% higher than that of commercial Pt/Vulcan, and this value is asserted to be compelling for higher electroactivity. The Pt/Vulcan by ethylene glycol has an ECSA value 40% higher than that of commercial Pt/Vulcan. This results support TEM results showing improved Pt dispersion with smaller Pt particle size and catalytic activity for all Pt/GNP, Pt/r-GO and Pt/Vulcan has enhanced.

Table 3-6. Calculated ECSA values of various GNP/Pt and GO/Pt

Sample	**ECSA (m^2/ g)**
Pt/r-GO by ethylene glycol reflux	**148**
Pt/r-GO by $NaBH_4$ reduction	17
Pt/r-GO by ascorbic acid reduction	34
Pt/GNP by ethylene glycol reflux	**85**
Pt/GNP by $NaBH_4$ reduction	22
Pt/GNP by ascorbic acid reduction	51
Pt/Vulcan (commercial 20% w:w)	**95**
Pt/Vulcan by ethylene glycol reflux	**134**
Pt/r-GO by ethylene glycol reflux (K_2PtCl_4)	60
Pt/TRGO by ethylene glycol reflux (H_2PtCl_6)	**135**
Pt/TRGO by ethylene glycol reflux (K_2PtCl_4)	70

3.6. In-situ Fuel Cell Testing Results

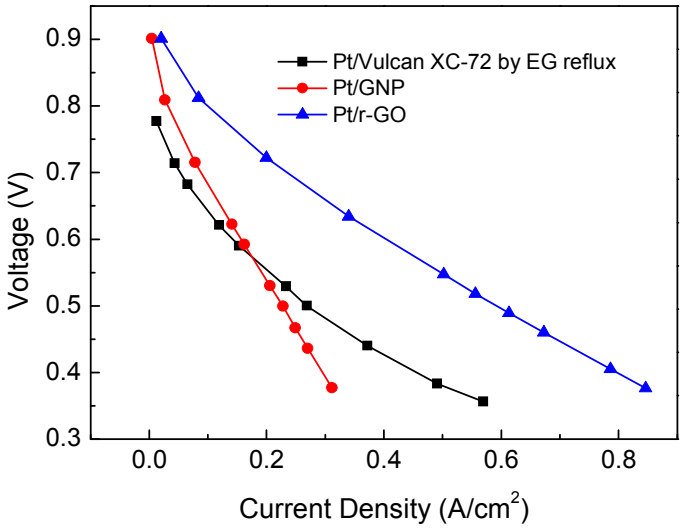

Figure 3-16. Polarization curves taken at 60°C

Fuel cell performance tests were conducted at 60°C with both anode and cathode containing synthesized Pt/r-GO, Pt/GNP and Pt/Vulcan XC-72 electrode. The polarization curves taken out of this measurements are shown in Figure 3-16. The Pt/GNP has a high open circuit voltage, however, the maximum current density that Pt/GNP can reach is relatively low compared to the other samples. The low amount of Pt nanoparticles attached on the surface of the GNP surface which has less Pt anchoring groups, results with a lower fuel cell performance. This result is supported with ECSA calculations in Table 3-6 out of CV measurements showing low Pt utilization of GNP.

Pt/r-GO electrodes demonstrates a superior performance over Pt/GNP and Pt/Vulcan electrodes at high current densities due to its high electrical conductivity, better dispersion of Pt nanoparticles on GO and lower Pt particle size. The performance of Pt/r-GO makes GO a very strong candidate to replace Vulcan usage in electrode layers. The calculated values of maximum power density of Pt/r-GO and Pt/Vulcan is about 320 $mW.cm^{-2}$ and 202 $mW.cm^{-2}$ respectively. The 40% increase in power density reveals that graphene support has much higher catalytic activity than commercial Vulcan XC-72.

4. CONCLUSION AND FUTURE WORK

This study was attributed to the detailed investigation of Pt impregnation methods (sodium borohydride, ethylene glycol, and ascorbic acid) on various graphene supports (GNP, GO, TRGO). The quality of synthesized electrocatalysts nanoparticles were analyzed by structural, chemical, optical and electrochemical characterization methods. In addition, fuel cell performance tests were conducted in order to anticipate practical applications of synthesized materials in fuel cell electrode layers.

According to XRD characterization, Pt impregnation on catalysts supports was successful for all reduction methods, however, the intensity of characteristic Pt peaks revealed that the degree of impregnation differentiates in each method. XRD spectra of Pt/GNP samples prepared by ethylene glycol reflux contains the most intense Pt peaks among the samples utilized GNP as catalyst support. The average particle size of Pt nanoparticles was calculated with Debye-Scherer equation. Pt/GNP by ethylene glycol was found out to have a particle size of 6.3 nm and Pt/GNP by ascorbic acid had a particle size of 4.8 nm. The results of the particle size was further investigated with TEM micrographs. TEM results showed that ethylene glycol reflux and ascorbic acid reduction produced samples with better distribution and lower particle size compared to $NaBH_4$. In the comparison of synthesized electrocatalysts in which GO was used as catalyst support, Pt/r-GO by ethylene glycol reflux was concluded to have superior properties according to XRD and TEM results. The average article size of Pt inside this sample was calculated with Debye-Scherer equation and noted as 4.7 nm, and homogenous dispersion of Pt on r-GO surface was indicative about positive effect of ethylene glycol method on GO supports.

The most significant property of graphene supported electrocatalysts that investigated in this study was electrocatalytic activity concerning possible fuel cell application. CV tests were conducted and ECSA values for each sample were calculated. Pt/r-GO samples showed the highest electrocatalytic activity with immense ECSA (148 $m^2.g^{-1}$). ECSA of Pt/r-GO by ethylene glycol method was disclosed to be 55% higher than commercial Pt/Vulcan. Ethylene glycol method was also very effective when GNP and TRGO was used as catalyst support. In consideration of characterization results, the most compelling impregnation method was noted as ethylene glycol reflux and GO was functions better as a catalyst support for Pt due to having Pt anchoring functional groups on its surface.

In the next step of this study, in-situ fuel cell characterizations of samples were completed to conclude which method shows a higher fuel cell performance. According to polarization curves, maximum power densities of samples were calculated and compared with synthesized Pt/Vulcan by ethylene glycol reflux. Pt/r-GO has a maximum power density of 320 $mW.cm^{-2}$ and this value is 40% higher than maximum power density of synthesized Pt/Vulcan (202 $mW.cm^{-2}$).

The use of a single type of catalyst support (GO) was finalized to demonstrate higher catalytic activity and fuel cell performance compared to Pt/C when ethylene glycol reflux was conducted for Pt reduction. In literature, the combination of two or more type of carbon supports has exhibit a distinct improvement over single type of catalyst supports. The proposed Pt impregnation method, ethylene glycol reflux, was concluded to be quite effective for graphene based supports. The validity of this impregnation method will be examined for hybrid structures in which GO is combined with other carbon supports such as CB, CNT, PANI, PPy and carbon nanopowder.

The most promising hybrid structures in terms of fuel cell performance will be further analyzed in order to obtain optimum combination of hybrid structures. Another important challenge for fuel cell is the cost of MEA. One of the future work will be dedicated to diminishing the Pt amount inside the catalyst layer.

REFERENCES

1. Larminie, J., A. Dicks, and M.S. McDonald, *Fuel cell systems explained*. Vol. 2. 2003: Wiley Chichester.

2. Barbir, F., *Chapter 1 - 1. Introduction*, in *PEM Fuel Cells*, F. Barbir, Editor. 2005, Academic Press: Burlington. p. 1-16.

3. Yuan, X.-Z., *PEM Fuel Cell Fundamentals*, in *PEM Fuel Cell Electrocatalysts and Catalyst Layers*, J. Zhang, Editor. 2008, Springer-Verlag London. p. 1-87.

4. Litster, S. and G. McLean, *PEM fuel cell electrodes.* Journal of Power Sources, 2004. **130**(1–2): p. 61-76.

5. Kim, M., et al., *The preparation of Pt/C catalysts using various carbon materials for the cathode of PEMFC.* Journal of Power Sources, 2006. **163**(1): p. 93-97.

6. Ye, S., M. Hall, and P. He, *PEM Fuel Cell Catalysts: The Importance of Catalyst Support.* ECS Transactions, 2008. **16**(2): p. 2101-2113.

7. Yoon, Y.G., et al., *Effect of pore structure of catalyst layer in a PEMFC on its performance.* International Journal of Hydrogen Energy, 2003. **28**(6): p. 657-662.

8. Kinoshita, K., *Carbon: Electrochemical and Physicochemical Properties*. 1988: Wiley. 560.

9. Walker, P., *Chemistry and Physics of Carbon*. Vol. 16. 1981: CRC Press. 336.

10. Pantea, D., et al., *Electrical conductivity of thermal carbon blacks: Influence of surface chemistry.* Carbon, 2001. **39**(8): p. 1147-1158.

11. Chi Linh, D., et al., *Properties of Pt/C nanoparticle catalysts synthesized by electroless deposition for proton exchange membrane fuel cell.* Advances in Natural Sciences: Nanoscience and Nanotechnology, 2013. **4**(3): p. 035011.

12. Kim, H., J.-N. Park, and W.-H. Lee, *Preparation of platinum-based electrode catalysts for low temperature fuel cell.* Catalysis Today, 2003. **87**(1–4): p. 237-245.

13. Kim, I., et al., *Highly active 40 wt.% PtRu/C anode electrocatalysts for PEMFCs prepared by an improved impregnation method.* International Journal of Hydrogen Energy, 2011. **36**(2): p. 1803-1812.

14. Iijima, S., *Helical microtubules of graphitic carbon.* Nature, 1991. **354**(6348): p. 56-58.

15. Li, W., et al., *Carbon nanotubes as support for cathode catalyst of a direct methanol fuel cell.* Carbon, 2002. **40**(5): p. 791-794.

16. Li, W., et al., *Preparation and Characterization of Multiwalled Carbon Nanotube-Supported Platinum for Cathode Catalysts of Direct Methanol Fuel Cells.* The Journal of Physical Chemistry B, 2003. **107**(26): p. 6292-6299.

17. Li, W., et al., *Homogeneous and controllable Pt particles deposited on multi-wall carbon nanotubes as cathode catalyst for direct methanol fuel cells.* Carbon, 2004. **42**(2): p. 436-439.

18. Lee, K., et al., *Progress in the synthesis of carbon nanotube- and nanofiber-supported Pt electrocatalysts for PEM fuel cell catalysis.* Journal of Applied Electrochemistry, 2006. **36**(5): p. 507-522.

19. Rajalakshmi, N., et al., *Performance of polymer electrolyte membrane fuel cells with carbon nanotubes as oxygen reduction catalyst support material.* Journal of Power Sources, 2005. **140**(2): p. 250-257.

20. Joo, S.H., et al., *Ordered nanoporous arrays of carbon supporting high dispersions of platinum nanoparticles.* Nature, 2001. **412**(6843): p. 169.

21. Ambrosio, E.P., et al., *Platinum catalyst supported on mesoporous carbon for PEMFC.* International Journal of Hydrogen Energy, 2008. **33**(12): p. 3142-3145.

22. Shanahan, P.V., et al., *Graphitic mesoporous carbon as a durable fuel cell catalyst support.* Journal of Power Sources, 2008. **185**(1): p. 423-427.

23. Viva, F.A., et al., *Mesoporous carbon as Pt support for PEM fuel cell.* International Journal of Hydrogen Energy, 2014. **39**(16): p. 8821-8826.

24. Gurunathan, K., et al., *Electrochemically synthesised conducting polymeric materials for applications towards technology in electronics, optoelectronics and energy storage devices.* Materials Chemistry and Physics, 1999. **61**(3): p. 173-191.

25. Park, J.-H., et al., *A novel direct deposition of Pt catalysts on Nafion impregnated with polypyrrole for PEMFC.* Electrochimica Acta, 2004. **50**(2–3): p. 769-775.

26. Zhongwei, C., et al., *Polyaniline nanofibre supported platinum nanoelectrocatalysts for direct methanol fuel cells.* Nanotechnology, 2006. **17**(20): p. 5254.

27. Yuan, X., et al., *Use of polypyrrole in catalysts for low temperature fuel cells.* Energy & Environmental Science, 2013. **6**(4): p. 1105-1124.

28. Novoselov, K.S., et al., *Electric field effect in atomically thin carbon films.* Science, 2004. **306**(5696): p. 666-9.

29. Hur, S.H. and J.-N. Park, *Graphene and its application in fuel cell catalysis: a review.* Asia-Pacific Journal of Chemical Engineering, 2013. **8**(2): p. 218-233.

30. Fampiou, I. and A. Ramasubramaniam, *CO Adsorption on Defective Graphene-Supported Pt13 Nanoclusters.* The Journal of Physical Chemistry C, 2013. **117**(39): p. 19927-19933.

31. Kou, R., et al., *Enhanced activity and stability of Pt catalysts on functionalized graphene sheets for electrocatalytic oxygen reduction.* Electrochemistry Communications, 2009. **11**(5): p. 954-957.

32. Shao, Y., et al., *Highly durable graphene nanoplatelets supported Pt nanocatalysts for oxygen reduction.* Journal of Power Sources, 2010. **195**(15): p. 4600-4605.

33. Novoselov, K.S., et al., *Two-dimensional atomic crystals.* Proceedings of the National Academy of Sciences of the United States of America, 2005. **102**(30): p. 10451-10453.

34. Nandamuri, G., S. Roumimov, and R. Solanki, *Chemical vapor deposition of graphene films.* Nanotechnology, 2010. **21**(14): p. 145604.

35. Brodie, B.C., *Sur le poids atomique du graphite.* Ann.Chim.Phys., 1860. **59**: p. 466-472.

36. Staudenmaier, L., *Verfahren zur Darstellung der Graphitsäure.* Berichte der deutschen chemischen Gesellschaft, 1898. **31**(2): p. 1481-1487.

37. Hummers, W.S. and R.E. Offeman, *Preparation of Graphitic Oxide.* Journal of the American Chemical Society, 1958. **80**(6): p. 1339-1339.

38. Marcano, D.C., et al., *Improved Synthesis of Graphene Oxide.* ACS Nano, 2010. **4**(8): p. 4806-4814.

39. Stankovich, S., et al., *Synthesis of graphene-based nanosheets via chemical reduction of exfoliated graphite oxide.* Carbon, 2007. **45**(7): p. 1558-1565.

40. Wang, G., et al., *Facile Synthesis and Characterization of Graphene Nanosheets.* The Journal of Physical Chemistry C, 2008. **112**(22): p. 8192-8195.

41. Saner, B., F. Okyay, and Y. Yürüm, *Utilization of multiple graphene layers in fuel cells. 1. An improved technique for the exfoliation of graphene-based nanosheets from graphite.* Fuel, 2010. **89**(8): p. 1903-1910.

42. Ramachandran, R., et al., *Synthesis of graphene platelets by chemical and electrochemical route.* Materials Research Bulletin, 2013. **48**(10): p. 3834-3842.

43. Fan, Z.-J., et al., *Facile Synthesis of Graphene Nanosheets via Fe Reduction of Exfoliated Graphite Oxide.* ACS Nano, 2011. **5**(1): p. 191-198.

44. Geng, J., et al., *A Simple Approach for Preparing Transparent Conductive Graphene Films Using the Controlled Chemical Reduction of Exfoliated Graphene Oxide in an Aqueous Suspension.* The Journal of Physical Chemistry C, 2010. **114**(34): p. 14433-14440.

45. Wan, L., et al., *Graphene nanosheets based on controlled exfoliation process for enhanced lithium storage in lithium-ion battery.* Diamond and Related Materials, 2011. **20**(5–6): p. 756-761.

46. Chen, G., et al., *Preparation and characterization of graphite nanosheets from ultrasonic powdering technique.* Carbon, 2004. **42**(4): p. 753-759.

47. Shao, Y., et al., *Facile and controllable electrochemical reduction of graphene oxide and its applications.* Journal of Materials Chemistry, 2010. **20**(4): p. 743-748.

48. Xin, Y., et al., *Preparation and characterization of Pt supported on graphene with enhanced electrocatalytic activity in fuel cell.* Journal of Power Sources, 2011. **196**(3): p. 1012-1018.

49. Li, F., et al., *Platinum nano-catalysts deposited on reduced graphene oxides for alcohol oxidation.* Electrochimica Acta, 2013. **111**(0): p. 614-620.

50. Zhang, S., et al., *Stabilization of platinum nanoparticle electrocatalysts for oxygen reduction using poly(diallyldimethylammonium chloride).* Journal of Materials Chemistry, 2009. **19**(42): p. 7995-8001.

51. Qiu, J.-D., et al., *Controllable Deposition of Platinum Nanoparticles on Graphene As an Electrocatalyst for Direct Methanol Fuel Cells.* The Journal of Physical Chemistry C, 2011. **115**(31): p. 15639-15645.

52. Park, J.Y. and S. Kim, *Preparation and electroactivity of polymer-functionalized graphene oxide-supported platinum nanoparticles catalysts.* International Journal of Hydrogen Energy, 2013. **38**(14): p. 6275-6282.

53. Yang, J., et al., *An effective strategy for small-sized and highly-dispersed palladium nanoparticles supported on graphene with excellent performance for*

formic acid oxidation. Journal of Materials Chemistry, 2011. **21**(10): p. 3384-3390.

54. Mondal, A. and N.R. Jana, *Surfactant-Free, Stable Noble Metal–Graphene Nanocomposite as High Performance Electrocatalyst.* ACS Catalysis, 2014. **4**(2): p. 593-599.

55. Zhang, Y., et al., *The simple preparation of graphene/Pt nanoparticles composites and their electrochemical performance.* Journal of Materials Science: Materials in Electronics, 2013. **24**(9): p. 3244-3248.

56. Li, Y., et al., *Catalytic performance of Pt nanoparticles on reduced graphene oxide for methanol electro-oxidation.* Carbon, 2010. **48**(4): p. 1124-1130.

57. Marinkas, A., et al., *Graphene as catalyst support: The influences of carbon additives and catalyst preparation methods on the performance of PEM fuel cells.* Carbon, 2013. **58**(0): p. 139-150.

58. Hsieh, S.H., et al., *Study of Pt catalyst on graphene and its application to fuel cell.* Applied Surface Science, 2013. **277**(0): p. 223-230.

59. Jehng, J.-M., et al., *Preparation of Pt nanoparticles on different carbonaceous structure and their applications to methanol electro-oxidation.* Applied Surface Science, 2013. **268**(0): p. 425-431.

60. Jung, J.H., et al., *Highly durable Pt/graphene oxide and Pt/C hybrid catalyst for polymer electrolyte membrane fuel cell.* Journal of Power Sources, 2014. **248**(0): p. 1156-1162.

61. Lei, M., et al., *Durable platinum/graphene catalysts assisted with polydiallyldimethylammonium for proton-exchange membrane fuel cells.* Electrochimica Acta, 2013. **113**(0): p. 366-372.

62. Zhang, M., et al., *Enhanced electrocatalytic activity of high Pt-loadings on surface functionalized graphene nanosheets for methanol oxidation.* International Journal of Hydrogen Energy, 2013. **38**(36): p. 16402-16409.

63. Taylor, E.J., E.B. Anderson, and N.R.K. Vilambi, *Preparation of high-platinum-utilization gas diffusion electrodes for proton-exchange-membrane fuel cells.* Journal of the Electrochemical Society, 1992. **139**(5): p. L45-L46.

64. Verbrugge, M.W., *Selective Electrodeposition of Catalyst within Membrane-Electrode Structures.* Journal of The Electrochemical Society, 1994. **141**(1): p. 46-53.

65. Anderson, E.B., N.R.K.V. Reddy, and J. Taylor, *High utilization supported catalytic metal-containing gas-diffusion electrode, process for making it, and cells utilizing it*. 1998, Google Patents.

66. Choi, K.H., H.S. Kim, and T.H. Lee, *Electrode fabrication for proton exchange membrane fuel cells by pulse electrodeposition.* Journal of Power Sources, 1998. **75**(2): p. 230-235.

67. Kim, H. and B.N. Popov, *Development of Novel Method for Preparation of PEMFC Electrodes.* Electrochemical and Solid-State Letters, 2004. **7**(4): p. A71-A74.

68. Kim, H., N.P. Subramanian, and B.N. Popov, *Preparation of PEM fuel cell electrodes using pulse electrodeposition.* Journal of Power Sources, 2004. **138**(1–2): p. 14-24.

69. Mitzel, J., et al., *Electrodeposition of PEM fuel cell catalysts by the use of a hydrogen depolarized anode.* International Journal of Hydrogen Energy, 2012. **37**(7): p. 6261-6267.

70. Yan, J., et al., *Electrochemical properties of graphene nanosheet/carbon black composites as electrodes for supercapacitors.* Carbon, 2010. **48**(6): p. 1731-1737.

71. Wang, Y., et al., *Graphene/carbon black hybrid film for flexible and high rate performance supercapacitor.* Journal of Power Sources, 2014. **271**(0): p. 269-277.

72. Park, S., et al., *Design of graphene sheets-supported Pt catalyst layer in PEM fuel cells.* Electrochemistry Communications, 2011. **13**(3): p. 258-261.

73. Lv, R., E. Cruz-Silva, and M. Terrones, *Building complex hybrid carbon architectures by covalent interconnections: graphene-nanotube hybrids and more.* ACS Nano, 2014. **8**(5): p. 4061-9.

74. Cheng, Q., et al., *Graphene and carbon nanotube composite electrodes for supercapacitors with ultra-high energy density.* Physical Chemistry Chemical Physics, 2011. **13**(39): p. 17615-17624.

75. Jha, N., et al., *Graphene-multi walled carbon nanotube hybrid electrocatalyst support material for direct methanol fuel cell.* International Journal of Hydrogen Energy, 2011. **36**(12): p. 7284-7290.

76. Brandon, D. and W.D. Kaplan, *Diffraction Analysis of Crystal Structure*, in *Microstructural Characterization of Materials*. 2008, John Wiley & Sons, Ltd. p. 55-122.

77. *Powder Diffraction : Theory and Practice*. 2008, Cambridge, GBR: Royal Society of Chemistry.

78. Kaidanovych, Z., Kalishyn, Y., Strizhak, P., *Deposition of Monodisperse Platinum Nanoparticles of Controlled Size on Different Supports.* Advances in Nanoparticles, 2013. **2**: p. 32-38.

79. Sakintuna, B., Y. Yürüm, and S. Çetinkaya, *Evolution of Carbon Microstructures during the Pyrolysis of Turkish Elbistan Lignite in the Temperature Range 700−1000 °C.* Energy & Fuels, 2004. **18**(3): p. 883-888.

80. Zhang, S.-L., *Raman Spectroscopy and Its Application in Nanostructures (2nd Edition)*. 2012, Hoboken, NJ, USA: John Wiley & Sons.

81. Brandon, D. and W.D. Kaplan, *Chemical Analysis of Surface Composition*, in *Microstructural Characterization of Materials*. 2008, John Wiley & Sons, Ltd. p. 423-455.

82. Ferraro, J.R., K. Nakamoto, and C.W. Brown, *Introductory Raman Spectroscopy*. 2002, Burlington, MA, USA: Academic Press.

83. Silverstein, R.M., F.X. Webster, and D. Kiemle, *Spectrometric Identification of Organic Compounds, 7th Edition*. 2005: Wiley Global Education.

84. Perkins, W.D., *Fourier transform-infrared spectroscopy: Part l. Instrumentation.* Journal of Chemical Education, 1986. **63**(1): p. A5.

85. Brandon, D. and W.D. Kaplan, *Transmission Electron Microscopy*, in *Microstructural Characterization of Materials*. 2008, John Wiley & Sons, Ltd. p. 179-260.

86. Williams, D.B., Carter, C. Barry, *Transmission Electron Microscopy*. 2 ed. 2009: Springer US.

87. Rouquerol, F., J. Rouquerol, and K.S.W. Sing, *Adsorption by Powders and Porous Solids : Principles, Methodology and Applications*. 1998, London, GBR: Academic Press.

88. Barbir, F., *PEM Fuel Cells: Theory and Practice*. 2nd Edition ed. 2013: Academic Press.

89. Villagrasa, J.P., J. Colomer-Farrarons, and P.L. Miribel, *Bioelectronics for Amperometric Biosensors*. State of the Art in Biosensors - General Aspects. 2013.

90. Marken, F., *Cyclic Voltammetry*, in *Electroanalytical Methods*, F. Scholz, Editor. 2002, Springer-Verlag Berlin Heidelberg.

91. Girishkumar, G., et al., *Single-wall carbon nanotube-based proton exchange membrane assembly for hydrogen fuel cells.* Langmuir, 2005. **21**(18): p. 8487-94.

92. Zhang, J., et al., *High temperature PEM fuel cells.* Journal of Power Sources, 2006. **160**(2): p. 872-891.

93. Sawant, S.Y., et al., *A low temperature bottom-up approach for the synthesis of few layered graphene nanosheets via C-C bond formation using a modified Ullmann reaction.* RSC Advances, 2015. **5**(58): p. 46589-46597.

94. Wang, S., et al., *Wettability and Surface Free Energy of Graphene Films.* Langmuir, 2009. **25**(18): p. 11078-11081.

95. Ferrari, A.C. and J. Robertson, *Interpretation of Raman spectra of disordered and amorphous carbon.* Physical Review B, 2000. **61**(20): p. 14095-14107.

96. Pullini, D., et al., *Enhancing the capacitance and active surface utilization of supercapacitor electrode by graphene nanoplatelets.* Composites Science and Technology, 2015. **112**(0): p. 16-21.

97. Mishra, A.K. and S. Ramaprabhu, *Palladium nanoparticles decorated graphite nanoplatelets for room temperature carbon dioxide adsorption.* Chemical Engineering Journal, 2012. **187**(0): p. 10-15.

98. Stuart, B.H., *Infrared Spectroscopy: Fundamentals and Applications*. 2004: John Wiley & Sons.

99. Nasrollahzadeh, M., et al., *Synthesis, characterization, structural, optical properties and catalytic activity of reduced graphene oxide/copper nanocomposites.* RSC Advances, 2015. **5**(14): p. 10782-10789.

100. Sharma, S., et al., *Rapid Microwave Synthesis of CO Tolerant Reduced Graphene Oxide-Supported Platinum Electrocatalysts for Oxidation of Methanol.* The Journal of Physical Chemistry C, 2010. **114**(45): p. 19459-19466.

101. Shen, P.K., et al., *Electro-oxidation of Methanol on NiO-Promoted Pt/C and Pd/C Catalysts.* Electrochemical and Solid-State Letters, 2006. **9**(2): p. A39-A42.

102. Lee, Y.-J., et al., *Dealloyed Pt2Os nanoparticles for enhanced oxygen reduction reaction in acidic electrolytes.* Applied Catalysis B: Environmental, 2014. **150–151**(0): p. 636-646.

103. Gutes, A., et al., *Graphene decoration with metal nanoparticles: Towards easy integration for sensing applications.* Nanoscale, 2012. **4**(2): p. 438-440.

104. Giovanni, M., et al., *Noble metal (Pd, Ru, Rh, Pt, Au, Ag) doped graphene hybrids for electrocatalysis.* Nanoscale, 2012. **4**(16): p. 5002-5008.

105. Simonov, P.A., et al., *Electrochemical behaviour of quasi-graphitic carbons at formation of supported noble metal catalysts*, in *Studies in Surface Science and Catalysis*, P.A.J.R.M.J.A.M.P.G. B. Delmon and G. Poncelet, Editors. 1998, Elsevier. p. 15-30.

106. Kudin, K.N., et al., *Raman Spectra of Graphite Oxide and Functionalized Graphene Sheets*. Nano Letters, 2008. **8**(1): p. 36-41.

107. Song, N.-J., et al., *Thermally reduced graphene oxide films as flexible lateral heat spreaders*. Journal of Materials Chemistry A, 2014. **2**(39): p. 16563-16568.